HHS Public Access

Author manuscript

Neuron. Author manuscript; available in PMC 2023 February 16.

Published in final edited form as:

Neuron. 2022 February 16; 110(4): 627–643.e9. doi:10.1016/j.neuron.2021.11.025.

Shed CNTNAP2 ectodomain is detectable in the cerebrospinal fluid and regulates Ca^{2+} homeostasis and network synchrony *via* PMCA2/ATP2B2

M. Dolores Martin-de-Saavedra[1], **Marc dos Santos**[1], **Lorenza Culotta**[1], **Olga Varea**[1], **Benjamin P. Spielman**[1], **Euan Parnell**[1], **Marc Forrest**[1], **Ruoqi Gao**[1], **Sehyoun Yoon**[1], **Emmarose McCoig**[1], **Hiba Jalloul**[1], **Kristoffer Myczek**[1], **Natalia Khalatyan**[2], **Elizabeth A. Hall**[2], **Liam S. Turk**[3,4], **Antonio Sanz-Clemente**[5], **Davide Comoletti**[3,4,6,7], **Stefan F. Lichtenthaler**[8,9,10], **Jeffrey Burgdorf**[1,11,12], **Maria Barbolina**[13], **Jeffrey N. Savas**[2], **Peter Penzes**[1,11,12,*]

[1]Department of Physiology, Northwestern University Feinberg School of Medicine, Chicago, IL 60611, USA

[2]Department of Neurology, Northwestern University Feinberg School of Medicine, Chicago, IL 60611, USA

[3]Child Health Institute of New Jersey, New Brunswick, NJ 08901, USA

[4]Department of Neuroscience and Cell Biology, Robert Wood Johnson Medical School, Rutgers, The State University New Jersey, New Brunswick, NJ 08901, USA

[5]Department of Pharmacology, Northwestern University Feinberg School of Medicine, Chicago, IL 60611, USA

[6]Department of Pediatrics, Robert Wood Johnson Medical School, Rutgers, The State University New Jersey, New Brunswick, NJ 08901, USA

[7]School of Biological Sciences, Victoria University of Wellington, Wellington 6140, New Zealand

[8]German Center for Neurodegenerative Diseases (DZNE), 81377 Munich, Germany

[*]Correspondence and Lead Contact: p-penzes@northwestern.edu.

AUTHOR CONTRIBUTIONS

MDMS, MdS, LC, OV, BPS, RG, MF, KM, NK, EAH, ASC, JB, MB and DC conducted experiments; PP, MDMS, MdS, OV, and JNS designed experiments; MDMS, MdS, PP, MB, SFL, and JNS analyzed the data; PP and MDMS conceptualized the research and wrote the paper.

DECLARATION OF INTERESTS

The authors declare no competing interests.

INCLUSION AND DIVERSITY STATEMENT

We worked to ensure gender balance in the recruitment of human subjects and to ensure diversity in experimental samples through cell line selection. One or more of the authors of this paper received support from a program designed to increase minority representation in science. The author list of this paper includes contributors from the location where the research was conducted who participated in the data collection, design, analysis, and/or interpretation of the work.

[9]Department of Neuroproteomics, School of Medicine, Klinikum rechts der Isar, and Institute for Advanced Study, Technical University of Munich, 81675 Munich, Germany

[10]Munich Cluster for Systems Neurology (SyNergy), 81377 Munich, Germany

[11]Center for Autism and Neurodevelopment, Northwestern University, Chicago, IL 60611, USA

[12]Department of Psychiatry and Behavioral Sciences, Northwestern University Feinberg School of Medicine, Chicago, IL 60611, USA

[13]Department of Biopharmaceutical Sciences, University of Illinois at Chicago, Chicago, IL 60607, USA.

SUMMARY

While many neuronal, membrane proteins undergo proteolytic cleavage, little is known about the biological significance of neuronal ectodomain shedding (ES). Here, we show that the neuronal sheddome is detectable in human cerebrospinal fluid (hCSF) and is enriched in neurodevelopmental disorder (NDD) risk factors. Among shed synaptic proteins was the ectodomain of CNTNAP2 (CNTNAP2-ecto), a prominent NDD risk factor. CNTNAP2 undergoes activity-dependent ES via MMP9 (matrix metalloprotease 9), and CNTNAP2-ecto levels are reduced in the hCSF of ASD individuals. Using mass spectrometry, we identified the PMCA Ca^{2+} extrusion pumps as novel CNTNAP2-ecto binding partners. CNTNAP2-ecto enhances the activity of PMCA2 and regulates neuronal network dynamics in a PMCA2-dependent manner. Our data underscore the promise of sheddome analysis in discovering neurobiological mechanisms, provide insight into the biology of ES and its relationship with the CSF, and reveal a mechanism of regulation of Ca^{2+} homeostasis and neuronal network synchrony by a shed ectodomain.

eTOC Blurb

Martin-de-Saavedra *et al.*, report that the neuronal sheddome is detectable in human cerebrospinal fluid and is enriched in neurodevelopmental disorder risk factors. Among them is the CNTNAP2 ectodomain. Its synaptic shedding is increased by neuronal activity. CNTNAP2-ecto binds and activates PMCA Ca^{2+} extrusion pumps and thereby decreases neuronal network synchrony.

Keywords

ectodomain shedding; autism; schizophrenia; cerebrospinal fluid; sheddome; CNTNAP2; calcium; network dynamics; proteomics; bioinformatics

INTRODUCTION

Numerous membrane-anchored proteins undergo proteolytic processing resulting in the release of a soluble extracellular fragment in a process called ectodomain shedding (ES) (Lichtenthaler et al., 2018). Specifically, several neuronal and synaptic proteins undergo ES, such as amyloid-β precursor protein (APP), neuroligin, and neurexin, among others. ES is regulated by neuronal activity (Lim et al., 2012; Peixoto et al., 2012; Sonderegger and Matsumoto-Miyai, 2014), and the activity of proteases such as MMP9 increases upon neuronal activity, i.e., long-term potentiation (Nagy et al., 2006).

ES plays a widespread role in the development and physiology of the central nervous system (Lichtenthaler *et al.*, 2018). For many synaptic adhesion molecules, proteolytic cleavage terminates adhesion, causing synapse weakening (Peixoto *et al.*, 2012; Suzuki et al., 2012). However, recently it has become clear that soluble shed ectodomains diffuse away from the site of origin and may act as paracrine signals. Only a handful of such examples are known so far, including shed α-neurexin promoting retrograde synaptic inhibition through calcium channel α2δ subunits (Tong et al., 2017). On the other hand, dysregulated neuronal ES has been linked to neurological diseases, including Alzheimer's disease (Haass et al., 2012), prion disease (Altmeppen et al., 2015), and inflammation (McIlwain et al., 2012).

Several proteomic analyses of secretomes and sheddomes have been performed (Kuhn et al., 2012; Thouvenot et al., 2012). The term "secretome" refers to all proteins found in the extracellular milieu of a given biological sample. The subset of proteins that underwent ES in the secretome is called the "sheddome." Thus, proteins in the sheddome originally possessed transmembrane domains or glycosylphosphatidylinositol (GPI) anchors. Sheddome analyses have led to curated databases for shed proteins (Tien et al., 2017); yet, they have been used mainly to identify protease substrates (Kuhn *et al.*, 2012) and for describing the functions of proteases in neuronal regulation (Kuhn et al., 2016).

The cerebrospinal fluid (CSF) contains proteins derived from the brain, giving it the potential to offer a readout of normal and pathophysiological processes in the brain of living humans. Remarkably, some synaptic membrane proteins are altered in the CSF of neuropsychiatric patients (Duits et al., 2018; Kester et al., 2015), and it is possible that synapse health may be monitored by analyzing synaptic proteins in the CSF (Bereczki et al., 2017). Despite the remarkable research and clinical opportunities offered by investigating the synaptic sheddome, a number of critical questions remain unanswered. For example, the contribution of synaptic proteins to the neuronal sheddome and its relationship with the CSF sheddome, and the physiological functions of synaptic ES are only beginning to be uncovered.

Contactin-associated protein-like 2 (CNTNAP2), encoded by the *CNTNAP2* gene, is a cell adhesion molecule from the neurexin superfamily. It is abundant in the brain, and it is enriched at synapses (Bakkaloglu et al., 2008). Gene dosage as well as rare and common variations in the *CNTNAP2* gene have been associated with several syndromal neurodevelopmental disorders (NDDs) sharing symptoms of epilepsy, intellectual disability (ID), ASD, and language impairment (Poot, 2015). Several members of the neurexin superfamily have been shown to undergo ES; however, it is unknown whether CNTNAP2 generates a soluble ectodomain with biological properties.

We hypothesized that proteomic and bioinformatic analysis of the CSF and neuronal sheddomes could reveal novel neurobiological functions and mechanisms. Our data underscore the power of sheddome analysis to identify novel neurobiological mechanisms, provide new insight into the biology of synaptic ES and its relationship to the CSF, and reveal a new regulation mechanism of Ca^{2+} homeostasis and neuronal network dynamics by a shed ectodomain.

RESULTS

The neuronal sheddome is detectable in the CSF and is enriched in NDD risk factors

To gain biological insight into the neuronal sheddome, we analyzed a published dataset from media obtained from cultured neurons (Kuhn *et al.*, 2016). The analyzed neuronal secretome contained both secreted and proteolytically released proteins. To determine the subset of secretome proteins that undergo ES, we computationally selected membrane-anchored proteins according to UniProt annotations. We identified 178 proteins that putatively undergo ES, defined here as the “neuronal sheddome” (Fig. 1A). Gene ontology (GO) analysis of the neuronal sheddome dataset revealed that the most enriched biological processes were “positive regulation of synapse assembly” and “cell adhesion.” Also enriched were “oligosaccharide metabolism” and axonal processes.

Soluble ectodomains shed into the neuronal milieu of the brain can diffuse into the CSF, suggesting that a portion of the neuronal sheddome could be detectable in the CSF. We computationally overlapped a published hCSF dataset with a dataset of membrane-anchored proteins according to UniProt annotations, yielding 161 proteins, designated as the “CSF sheddome” (Fig. 1B). GO analysis revealed “cell adhesion” and “axon guidance” as the most significantly enriched biological processes, along with “nervous system development”, “adult locomotor behavior”, and “positive regulation of synapse assembly.” Furthermore, when analyzed by number of proteins per biological process, “cell adhesion” was the most highly represented in the neuronal sheddome and hCSF datasets with “axonogenesis” and “positive regulation of synapse assembly” being among the top four (Fig. S1A). In contrast, GO analysis of soluble proteins released by secretion in the neuronal secretome and the hCSF showed an enrichment in processes less related to neuronal regulation, such as “extracellular matrix organization” and “platelet degranulation” (Fig. S1B).

We examined the disease risk factor profiles of the neuronal secretome and the hCSF. We overlapped separately the membrane-anchored (sheddome) or the soluble secreted protein lists with NDD risk genes. Remarkably, proteins encoded by ASD susceptibility genes were significantly enriched in the neuronal sheddome, but not in the soluble component of the neuronal secretome (Fig. 1C). Similarly, ASD and schizophrenia (SZ) risk-gene-encoded proteins were enriched in the cleaved hCSF, but not in the soluble fraction (Fig. 1D). We corroborated this enrichment in ASD-related genes by performing the same analysis using the ASD risk genes annotated by SFARI (Fig. S1C). This indicates an enrichment in NDD risk factors in both the neuronal and CSF sheddomes.

The presence of putative shed ectodomains of numerous proteins in both the neuronal sheddome and the hCSF, as well as the similarity in their GO and disease profiles, suggested that a fraction of the ectodomain species from the neuronal sheddome could be detected in the hCSF. To test this hypothesis, we performed two different analyses. First, hypergeometric testing showed a significant overlap between the neuronal sheddome and the hCSF sheddome (Fig. 1E). Second, we found a significant correlation between the spectral counts of membrane-bound proteins in the neuronal secretome and in the CSF (Fig. 1F). Interestingly, we did not find a significant correlation in the soluble protein

component between these two data sets. These results indicate that a subset of neuronal shed ectodomains can be detected in the hCSF.

We hypothesized that a fraction of the synaptic sheddome may also be detectable in hCSF. On overlapping the hCSF dataset and the postsynaptic density (PSD) proteome, we found that 54 of 1,408 PSD proteins (~4%) were detected in the hCSF sheddome (Fig. 1G). We built a protein-protein interaction (PPI) network from these 54 proteins and highlighted the ones implicated in ASD, cell adhesion, and neurodevelopment, based on our computational analysis (Fig. 1H). This PPI network includes several NDD-associated synaptic molecules already known to undergo ES (such as NRXN1/3 and L1CAM), supporting our hypothesis. Remarkably, it also includes many NDD-associated and synaptic proteins not yet reported to undergo ES, including CNTNAP2. This highlights the paucity of information on ES and suggests that analysis of the CSF could be a promising strategy to investigate synaptic ES in humans.

CNTNAP2 undergoes ectodomain shedding

To further explore the hypothesis that analysis of the synaptic sheddome can reveal novel neurobiological mechanisms, we focused our investigation on CNTNAP2. We validated the presence of CNTNAP2-ecto in hCSF and mouse CSF (mCSF) by western blotting (WB), using antibodies against the extracellular N-terminal (N-term) region and the intracellular C-terminal (C-term) region. The N-term-directed antibody detected a band in both hCSF and mCSF, with a molecular weight just below that of the full-length protein containing the C-term region, suggesting that CNTNAP2-ecto was the product of cleavage of the full-length protein (Fig. 2A). To corroborate that the protein we detected in hCSF corresponds to CNTNAP2-ecto, we examined two published datasets of peptide mapping of CSF proteins analyzed by MS and did not detect any peptides corresponding to the intracellular domain of CNTNAP2 (Chiasserini et al., 2014; Macron et al., 2018). Similarly, only peptides corresponding to the extracellular domains were present for two other proteins known to undergo ES, NLGN1 and APP (Fig. S2A) suggesting that none of the proteins were originating from extracellular vesicles or cell debris.

Analysis by WB revealed CNTNAP2-ecto existed in the soluble fraction from wild-type (WT) mice but not in the *Cntnap2* knockout (KO) mice (Fig. 2B). Conversely, the full-length CNTNAP2 was detectable in the cortical membrane fraction but not in the soluble fraction of WT mice. We also detected the shorter CNTNAP2-ecto, but not the full-length CNTNAP2, in the extracellular media from WT but not *Cntnap2* KO mouse cortical neuronal cultures (Fig. 2C). We then measured CNTNAP2-ecto levels in hCSF from unaffected controls and individuals with ASD using the N-term antibody combined with enzyme-linked immune-sorbent assay (ELISA) and found a 35% decrease in CNTNAP2-ecto levels in individuals with ASD (Fig. 2D).

Taken together, these data show that CNTNAP2-ecto can be detected in the CSF, in neuronal culture media, and in the soluble fraction of the mouse cortex. Moreover, its levels are reduced in the CSF of individuals with ASD.

Spatial distribution of CNTNAP2 ectodomain shedding in synaptodendritic regions

To distinguish CNTNAP2-ecto on the cell surface and in the perineuronal space from full-length CNTNAP2, we immunostained for Flag in non-permeabilized neurons (surface Flag), followed by permeabilization and immunostaining with the C-term antibody (Fig. (plasmid validation Fig. S3B–D). Confocal imaging followed by 3D reconstructions showed surface Flag immunofluorescence outside of transfected cells and on the cell surface; this colocalized with C-term immunofluorescence only at the cell surface (Fig. 3A, blue arrowheads) but not in the perineuronal space (Fig. 3A, red arrowheads). Signal from surface and total CNTNAP2 were absent in non-transfected cells (Fig. S3A).

Then, we overexpressed Flag-CNTNAP2 in *Cntnap2* KO (KO tfx) mouse neurons and immunostained for Flag, C-term CNTNAP2, and the presynaptic glutamatergic marker vGLUT1. Confocal imaging analysis showed that the mean intensity of the extracellular CNTNAP2-ecto puncta colocalizing with vGLUT1 was significantly higher than that of all extracellular CNTNAP2-ecto puncta (Fig. 3B–C), indicating an apparent accumulation at presynaptic targets. These data indicate that CNTNAP2 is shed; the shed ectodomain localizes extracellularly near dendritic and synaptic regions, often targeting presynaptic sites.

CNTNAP2 ectodomain shedding increases with neuronal activity and is dependent on MMPs

Because cleavage of several synaptic adhesion molecules is regulated by neuronal activity (Conant et al., 2015), we examined the effect of chemical long-term potentiation (cLTP) on CNTNAP2-ecto production. Induction of cLTP in 4-week-old cultures resulted in an increase in CNTNAP2-ecto in the neuronal extracellular media (ECM) but not in whole cell lysates (WCLs) (Fig. 4A, S4A–B), indicating that CNTNAP2-ecto shedding is up-regulated during synaptic potentiation. ES enhancement by cLTP required both NMDA and AMPA receptor activity, as it was blocked by both 2-amino-5-phosphonovalerate (APV) and 2,3-dioxo-6-nitro-7-sulfamoyl-benzo[f]quinoxaline (NBQX) (Fig. 4B). Using subcellular fractionation to examine the biochemical compartmentalization of activity-induced CNTNAP2 cleavage, we observed a decrease of CNTNAP2 levels in the synaptic fraction after cLTP, and no change in the extrasynaptic fraction (Fig. 4C), indicating that activity-dependent CNTNAP2 cleavage occurred in synaptic regions.

We then used protease inhibitors to identify the sheddases responsible for CNTNAP2 cleavage. CNTNAP2 ES induced by cLTP was blocked by TAPI-0, which inhibits several proteases, and by the general MMP inhibitor GM6001 (GM) (Fig. 4D). MMP9 inhibitor I blocked cLTP-dependent CNTNAP2-ecto shedding in a concentration-dependent manner (Fig. 4E), indicating that MMP9 mediates activity-dependent CNTNAP2-ecto shedding. To validate this *in vivo*, we injected mice with GM6001. After 4h of intraperitoneal administration of GM at 100 mg/kg, we found a significant reduction in CNTNAP2-ecto levels in cortical soluble fractions (Fig. 4F). We also found a 30% decrease in cortical soluble fractions of neuroligin-1 (NLGN1), known to undergo MMP9-dependent ES *in vivo* (Peixoto *et al.*, 2012), validating our model (Fig. S4C). To determine how increased neuronal activity in the brain affected CNTNAP2-ecto levels in the CSF, we subjected mice

to electroconvulsive shock (ECS), collected CSF 4 and 8h later, and analyzed it by WB. CNTNAP2-ecto in the CSF had tripled 8h after ECS (Fig. 4G). Taken together, these data indicate that CNTNAP2 ES is enhanced by neuronal activity and is mediated by MMPs.

Activity modulates CNTNAP2-ecto shedding and perineuronal distribution

We investigated the effect of cLTP on the spatial distribution of CNTNAP's shedding using similar method to those in "Spatial distribution of CNTNAP2 ectodomain shedding in synaptodendritic regions." Using structured illumination microscopy (SIM) imaging that allows for increased lateral resolution, we observed a significant increase in the number of ecto puncta outside the GFP signal in cLTP-subjected neurons (Fig. 5A–B). We also found a significant increase in the number of CNTNAP2-ecto puncta overlapping with vGLUT1 outside the transfected neuron after cLTP (Fig. 5A–C), suggesting that presynaptic sites were among the targets of neuronal-activity cleaved CNTNAP2.

We analyzed the overlap of activity-induced CNTNAP2-ecto with the GFP-outlined compartment after SIM imaging (Fig. 5D–F). We found no significant difference in the area occupied or the number of CNTNAP2-ecto puncta within the dendritic compartment between the control and cLTP-treated neurons (Fig. 5E). However, upon cLTP both the area occupied and the number of CNTNAP2-ecto puncta significantly decreased in the synaptic region, defined as the overlap between GFP and vGLUT1 (Fig. 5F). These data suggest that CNTNAP2-ecto produced postsynaptically upon cLTP diffuses away from postsynaptic regions.

CNTNAP2-ecto affinity-MS identifies PMCA2 as a novel interacting partner

Previous reports identified signaling roles for ectodomains (Grell et al., 1995; Prenzel et al., 1999), so we hypothesized that shed CNTNAP2-ecto may act as a ligand for unknown membrane proteins. To identify ecto-binding partners, we incubated Flag-CNTNAP2-ecto with mouse cortical membrane preparations, then comprehensively analyzed affinity-purified proteins by LC-MS/MS. To sort the identified proteins, we rank-ordered the prey proteins detected based on the number of normalized spectral counts, highlighting ASD-related risk factors and the positive control CNTN1 in green (Fig. 6A). As expected, the bait protein was the most abundant, while the known CNTNAP2-ecto interactor CNTN1 (Rubio-Marrero et al., 2016) was highly enriched, validating our approach. In addition, all four members of the plasma membrane Ca^{2+}-ATPase (PMCA) family of Ca^{2+} pumps were very abundant (Fig. 6B). SYPRO Ruby staining of CNTNAP2-ecto showed a highly pure bait sample, and MS analysis of tryptic peptide digestion of purified CNTNAP2-ecto indicated no contamination with the full-length protein (Fig. S5A–B).

Because PMCA2 showed a high enrichment and it has been implicated in ASD (Takata et al., 2018), we investigated its interaction with CNTNAP2-ecto. We immunoprecipitated PMCA2 from mouse cortex homogenates and detected both the full-length (N-term and C-term signals, above the 150 KDa marker) and the CNTNAP2-ecto (N-term signal only, below the 150 KDa marker) (Fig. 6C), indicating that both the full-length and the CNTNAP2-ecto interact with PMCA2. In addition, we mimicked the LC-MS/MS experiment, and validated the interaction between exogenous CNTNAP2-ecto and PMCA2

by WB (Fig. S5C). We then compared the protein levels of PMCA2 in WT and *Cntnap2* KO mouse cortices and found a significant reduction in PMCA2 levels in the KO at P28 (Fig. 6D). Finally, using confocal microscopy, we found an overlap of Flag with PMCA2 both within and outside of the GFP-outlined perimeter of the transfected neurons, indicating that the cleaved CNTNAP2-ecto may bind to PMCA2 on distal sites of the cell of origin (Fig. 6E). We found no colocalization between Flag and PMCA2 in *Cntnap2* KO neurons (Fig. S5D). These experiments indicate that PMCA2 is a novel binding partner of CNTNAP2-ecto.

PMCA2 regulates cytosolic Ca^{2+} by extruding Ca^{2+} into the extracellular space, so we analyzed whether CNTNAP2-ecto directly modulates PMCA2 activity. We expressed exogenous PMCA2 in HEK293 cells, incubated them with CNTNAP2-ecto, and we elicited a cytosolic Ca^{2+} signal with 0.5 mM ATP (Fig. 6F–G; protocol in Fig. S5E). CNTNAP2-ecto reduced the $t_{1/2}$ off by ~50%, without affecting non-transfected HEK293 cells (Fig. 6H). However, tau_{on} (Fig. 6I), Ca^{2+} peak amplitude, t_{max}, or area under the curve (AUC) (Fig. S5F) were not affected by CNTNAP2-ecto. This indicates that CNTNAP2-ecto increases Ca^{2+} extrusion in a PMCA2-dependent manner in HEK293 cells.

CNTNAP2-ecto enhances Ca^{2+} extrusion

We then assess the effect of CNTNAP2-ecto on KCl-induced Ca^{2+} signals in neuronal somata *in vitro*. (Fig.7A, protocol in Fig.S6A). Incubation with CNTNAP2-ecto decreased the $t_{1/2}$ off of the KCl-induced Ca^{2+} signal by 30% (Fig. 7B–D), without affecting tau_{on}, peak amplitude, or t_{max} (Fig. S6B). We examined the effect of incubation with CNTNAP2-ecto on KCl-elicited Ca^{2+} signals in dendrites and spines of cultured neurons by time-lapse confocal imaging (Fig. 7E). Incubation with CNTNAP2-ecto decreased the $t_{1/2}$ off of KCl-elicited Ca^{2+} peaks both in spines (Fig. 7F) and in dendrites (Fig. 7G). These data indicate that CNTNAP2-ecto increases the extrusion rate of cytosolic Ca^{2+} in somata, dendrites, and spines of primary neurons.

To investigate the effect of CNTNAP2-ecto in the context of native brain tissue, we measured KCl-evoked Ca^{2+} responses in acute brain slices in layer V of the secondary motor cortex (M2). After incubation with CNTNAP2-ecto, we imaged KCl-evoked Ca^{2+} peaks (Fig. 7H, I and Supplementary Video 1). CNTNAP2-ecto decreased $t_{1/2}$ off by 22% without affecting tau_{on} (Fig. 7J). This indicates that CNTNAP2-ecto enhances Ca^{2+} extrusion in acute brain slices.

We then incubated the neurons with CNTNAP2-ecto, or boiled CNTNAP2-ecto in PMCA2 knockdown conditions (validation of construct in Fig. S7) and imaged KCl-evoked Ca^{2+} signals as above (protocol in Fig. S6C). We detected a 30% decrease in $t_{1/2}$ off of the KCl-evoked Ca^{2+} for treatment with CNTNAP2-ecto *vs.* the boiled ecto, an effect that was absent in shPMCA2 neurons (Fig. 7K–M). These data show that CNTNAP2-ecto enhances Ca^{2+} extrusion in a PMCA2-dependent manner.

CNTNAP2-ecto regulates neuronal network dynamics

The coordinated activity of large numbers of neurons within networks and circuits are critical for cognition and behavior (Uhlhaas and Singer, 2006; 2007), and is implicated in

the pathophysiology of ASD and epilepsy (Uhlhaas and Singer, 2006). Due to CNTNAP2-ecto's ability to modulate Ca^{2+} homeostasis within individual neurons, we hypothesized that it could regulate neuronal functioning at the network level as well. Using two-photon microscopy, we measured spontaneous Ca^{2+} events in the CA3 region of the hippocampus of acute brain slices obtained from P5-P7 mice (Fig. 8A). We quantified synchrony as the fraction of synchronized transients, i.e., frames presenting a significantly higher number of co-active neurons than estimated by chance (Fig. S8A–E). As expected, vehicle-treated slices exhibited recurrent synchronized Ca^{2+} network events, observed as a higher number of neurons presenting simultaneous Ca^{2+} signals (Fig. 8B–C, Supplementary Video 2). Remarkably, CNTNAP2-ecto incubation decreased the fraction of synchronized Ca^{2+} transients by 30% (Fig. 8D). This was also evident in raster plots where neurons were color-coded for synchrony within a network event (Fig. 8C). Consistent with this, we found a 47% decrease in the number of Ca^{2+} network events/5 min upon CNTNAP2-ecto treatment (Fig. 8E). However, this was not associated with statistically significant changes in Ca^{2+} transient frequency per cell or Ca^{2+} amplitude (Fig. 8F–G). We observed similar effects of CNTNAP2-ecto on network activity in primary cortical neurons (Fig. S8F–I). We then analyzed ensembles of co-active neurons during synchronized network events. Fig. 8H shows three representative network events per condition, showing that CNTNAP2-ecto treatment reduced the percentage of co-active neurons during synchronized network events by 40% (Fig. 8I).

To determine whether the observed changes in Ca^{2+} network dynamics correspond to changes in electrical properties of neuronal networks, we employed microelectrode arrays (MEA) with neuronal cultures infected with a lentivirus expressing scrambled shRNA or PMCA2 shRNA (validation in Fig. S7, Fig. 8J). We detected a 26% decrease in the synchrony index of cortical neurons treated with CNTNAP2-ecto, while knockdown of PMCA2 prevented this effect (Fig. 8K). We also found a 49% decrease in network burst frequency upon CNTNAP2-ecto treatment (Fig. 8L). The decrease in network burst frequency was absent in neurons where PMCA2 was knocked down. Conversely, we did not find a significant difference in burst frequency or weighted mean firing rate in individual cells upon CNTNAP2-ecto treatment (Fig. S8J–K), indicating a network-level effect as opposed to a single-cell effect. Importantly, an unrelated ectodomain, contactin4-ecto, did not modify the synchrony index (Fig. S8L), suggesting the effects were specific for CNTNAP2-ecto. In summary, CNTNAP2-ecto alters neuronal circuit properties by reducing network synchrony in a PMCA2-dependent manner.

DISCUSSION

Our research revealed that a significant fraction of the proteins in the neuronal and synaptic sheddomes are detectable in the human CSF, and that the CSF sheddome is enriched in proteins encoded by NDD risk genes. We showed that a prominent NDD risk factor, CNTNAP2, undergoes activity-dependent ES, and the levels of its shed ectodomain are reduced in the CSF of individuals with ASD. Additionally, CNTNAP2-ecto interacted and enhanced the Ca^{2+} extrusion rate of PMCA2, a known ASD risk factor. Finally, we showed that CNTNAP2-ecto decreased neuronal network activity and synchrony in PMCA2-dependent manner. These findings highlight the promise of analyzing the neuronal

sheddome to discover novel neurobiological mechanisms, provide new insight into the biology of synaptic ES and its relationship to the CSF, and reveal a new mechanism of regulating Ca^{2+} homeostasis and neuronal synchrony by a shed ectodomain.

The neuronal sheddome is detectable in the CSF and is enriched in NDD risk factors

We used bioinformatics to analyze proteomic data to characterize the neuronal sheddome and understand its relationship with the CSF sheddome. We found that both the neuronal and the CSF sheddomes are enriched in proteins involved in cell adhesion and synapse assembly. This is somewhat unexpected, because synapses represent only a modest fraction of the central nervous system material, and the CSF is in contact with multiple cell types and tissues. Moreover, adhesion proteins represent only a fraction of all membrane proteins. We also show that there is a strong spectral count correlation between proteins detected in the neuronal sheddome and those in the CSF sheddome. Indeed, ~ 37% (66/161) of the neuronal sheddome was detectable in the CSF. Remarkably, ~ 34% (54/161) of the CSF sheddome proteins were potentially of synaptic origin, as shown by their presence in published PSD proteomic datasets. Interestingly, both the neuronal and CSF sheddomes were abundant in proteins encoded by ASD risk genes. There are several implications of these findings. First, ES seems much more prevalent than previously thought. Second, CSF analysis could provide substantial biochemical insight into synaptic ES in living organisms, including humans, and shed light into the effect of ES in entire pathways.

CNTNAP2 undergoes activity-dependent ectodomain shedding

CNTNAP2 was not previously known to undergo ES. Its cleavage is mediated by MMP9, which also mediates the activity-dependent cleavage of other synaptic proteins (Peixoto *et al.*, 2012; Tian et al., 2007). Moreover, CNTNAP2 ES was enhanced by neuronal activity and was dependent on glutamatergic transmission, as observed for other cell adhesion molecules (Nagappan-Chettiar et al., 2017). This activity-dependent regulation occurred *in vivo*, upon the induction of seizures and was detectable in the CSF. This data supports the idea that changes in ES in the brain could be detectable in the CSF.

Imaging revealed that CNTNAP2-ecto was present outside of neurons. Interestingly, cLTP resulted in reduced CNTNAP2-ecto in synaptic contact regions, and an increase at presynaptic sites. Similarly, postsynaptically released neurexin-1 ectodomains have shown presynaptic effects by binding to CaV2 Ca^{2+} channels and reducing acetylcholine release at the neuromuscular junction (Tong *et al.*, 2017). Synaptic ES may thus represent a general mechanism of intercellular signaling originating at synapses, but not mediated by classical neurotransmitters/neuromodulators.

A shed ectodomain is a novel extracellular regulator of PMCA2 activity and neuronal Ca^{2+} dynamics

CNTNAP2 was originally shown to regulate the localization of Shaker-like K^+ channels on myelinated axons (Poliak et al., 1999; Poliak et al., 2003). Its intracellular binding partners are reasonably well known (Gao et al., 2018; Gao et al., 2020; Horresh et al., 2008). However, CNTN2 and −1 were the only known partners for its extracellular domain (Poliak et al., 2003; Rubio-Marrero *et al.*, 2016). Affinity-based proteomic analysis allowed

us to identify novel interacting partners of CNTNAP2-ecto, being PMCA2 one of the most enriched interactors. Accurate control of intracellular Ca^{2+} is crucial for neuronal function, and the PMCA family of Ca^{2+} pumps are the most prominent Ca^{2+} extrusion mechanisms. PMCA2 is widely distributed throughout the brain (Fig. S5G) and is present both pre- and postsynaptically (Burette and Weinberg, 2007). Although intracellular regulators of PMCA2 activity are known (Brini and Carafoli, 2009; Niggli et al., 1981), CNTNAP2-ecto is the first reported extracellular activator of PMCA2.

A shed ectodomain regulates network synchrony

Synchronized neuronal network activity plays key roles during brain development, sensory processing, and cognition (Uhlhaas and Singer, 2010). Importantly, neuronal network synchrony alterations occur in NDDs including, ASD, SZ, and epilepsy (Mathalon and Sohal, 2015; McCormick and Contreras, 2001). Although the exact mechanisms remain obscure, synchronized network events are thought to arise from the interplay between synaptic connectivity, intrinsic excitability, and cell-type composition of the network (Alford and Alpert, 2014; Iida et al., 2018; Wong et al., 1984). We show that the effect of CNTNAP2-ecto on network activity depends on PMCA2. One mechanism could be through the modulation of Ca^{2+} extrusion. Indeed, intracellular [Ca^{2+}] is tightly linked to neuronal excitability and shapes global network activity (Lavi et al., 2015; Roussel et al., 2006). Asynchronous vesicle release, which is controlled by slow clearance of residual Ca^{2+} from the presynaptic terminal, is known to regulate network synchrony (Lavi *et al.*, 2015; Lavi et al., 2014). CNTNAP2-ecto could be increasing Ca^{2+} extrusion presynaptically, which in turn would decrease asynchronous vesicle release, thereby reducing network activity. However, as the MS data revealed numerous CNTNAP2-ecto interactors, it cannot be ruled out that the interaction with other binding partners could regulate CNTNAP2-ecto phenotypes.

CNTNAP2-ecto's effect on network dynamics could fulfill key physiological functions. Activity-regulated increase of CNTNAP2-ecto may mediate feedback inhibition in response to an increase in neuronal activity, such as following LTP. CNTNAP2-ecto shedding may act as a natural seizure-suppression mechanism by restricting excessive network activity, over-excitation and excessive synchrony. Neuronal synchrony has been hypothesized to play a major role in the coding and propagation of information throughout the brain (Panzeri et al., 2015). Higher synchrony is hypothesized to confer faster response and robustness of the information carried, whereas lower synchrony increases the efficiency of coding more information into a more complex spike code.

Clinical implications

We showed that the CSF contains a significant fraction of proteins present in the neuronal and synaptic sheddomes, and that changes in brain activity, such as seizures, are reflected in the CSF sheddome. Thus, analysis of the CSF may allow access to pathophysiological processes in the brain in live subjects. The abundance of specific ectodomains in the CSF may reflect the levels of protein expression, protease function, and neuronal activity affected in brain disorders or pharmacological treatments. Shed neuronal and synaptic proteins measured in the CSF could serve as biomarkers for such processes. Along these lines, in neurodegenerative disorders such as amyotrophic lateral sclerosis, Parkinson's disease, and

Alzheimer's disease, elevated levels of synaptic proteins in the CSF are thought to reflect synapse loss (Bereczki *et al.*, 2017; Collins et al., 2015; Jiao et al., 2015; Kester *et al.*, 2015; Khoonsari et al., 2016).

Interestingly, we found reduced CNTNAP2-ecto levels in CSF from individuals with ASD and increased CNTNAP2-ecto in mice subjected to ECS (ASD is often comorbid with epilepsy). PMCA2 genetic variation has also been implicated in ASD (Takata *et al.*, 2018); it has been observed that individuals with ASD present with reduced PMCA2 protein levels in brain tissue (Voineagu et al., 2011), and reduced mRNA levels in lymphoblasts (Stafford et al., 2017).

Alterations in neuronal synchrony are thought to occur in ASD, SZ, (Mathalon and Sohal, 2015), epilepsy (McCormick and Contreras, 2001), and also disorders associated with CNTNAP2 genetic variation (Scott-Van Zeeland et al., 2010). Abnormal synchrony has also been reported in multiple mouse models of NDDs, including *Cntnap2* KO mice (Penagarikano et al., 2011). As such, abnormal levels of CNTNAP2-ecto, either caused by anomalous CNTNAP2 expression or shedding, could cause altered network synchrony or seizure susceptibility.

STAR METHODS

Resource availability

Lead contact—Further information and requests for resources and reagents should be directed to and will be fulfilled by the Lead Contact, Peter Penzes (p-penzes@northwestern.edu).

Materials availability—This study did not generate new unique reagents. Further information and requests for materials should be directed to and will be fulfilled by the Lead Contact, Peter Penzes, upon request.

Data and code availability—Datasets, code or any additional information related to the current study are available from the Lead Contact, Peter Penzes, upon request.

Experimental model and subject

Cntnap2 knockout mice—*Cntnap2* KO mice were generated and kindly donated by Elior Peles (Weizmann Institute of Science, Israel). The colony was genotyped following the primers and conditions previously described (Poliak *et al.*, 2003), and it was maintained in the original strain, CD1. Mice were housed within a specific-pathogen-free (SPF) barrier area. Environmental parameters were controlled and monitored; temperatures were 72±2 °F. The humidity range was greater than 30%. Food and water (reverse osmosis water from an automatic water system) were provided *ad libitum*. All animal procedures were performed with the approval of the Institutional Animal Care and Use Committee (IACUC) at Northwestern University.

HEK293 cells—HEK293 cells were grown at 37 °C with 5% CO_2 in Dulbecco's modified Eagle's medium (DMEM, Thermo Fisher) containing 10% fetal bovine serum (Corning) and

penicillin/streptomycin (Sigma-Aldrich). They were passaged appropriately during the linear growth phase to maintain sub-confluent culture, twice per week.

Murine and hCSF samples for Western blot—Pooled murine (CD1) and remnants of human CSF (hCSF) were obtained from Bioreclamation IVT for Western blot analysis.

Human CSF samples used for ELISA—Unaffected controls and ASD postmortem hCSF samples used for ELISA analysis were obtained from the University of Maryland Brain and Tissue Bank (Baltimore, MD) on behalf of the NIH Neurobiobank. The characteristics of the subjects were as follows: unaffected controls; 5 females, 5 males, 1 n/a, ages 32.9±8.6 years old (mean±SEM); ASD, 6 females, 11 males, 1 n/a, ages 22.18±2.5 years old. There was no significant age difference between groups (P=0.13). Moreover, no correlation between CNTNAP2 CSF levels and age was observed either in unaffected controls or ASD samples (control: P=0.6988, ASD: P=0.72). No gender difference was found for CNTNAP2 CSF levels. All samples were negative for HIV and hepatitis.

Method details

Antibodies and plasmids—The following antibodies were purchased: CNTNAP2 (C-terminal, rabbit polyclonal, Millipore), CNTNAP2 (N-terminal, mouse monoclonal, Neuromab), actin (mouse monoclonal, Abcam), GFP (chicken polyclonal, Abcam), Flag (mouse monoclonal, Sigma-Aldrich), vGLUT1 (guinea pig polyclonal, Synaptic System Antibodies), PMCA2 (rabbit polyclonal, Thermo Fisher), β3-tubulin (rabbit monoclonal, Cell Signaling Technology), EEA1 (rabbit polyclonal, Cell Signaling Technology), PSD95 (rabbit monoclonal, Cell Signaling Technology), CaMKII, phospho Thr286 (rabbit polyclonal, Abcam), Neuroligin 1 (N-terminal, rabbit polyclonal, Alomone) and CNTN1 (N-terminal, goat polyclonal, Abcam). Plasmids used in this study were: pEGFP-N1 and DsRedExpress2 (Clontech); Flag-CNTNAP2 (generated by subcloning human CNTNAP2 cDNA from a plasmid kindly provided by Dr. Elior Peles, Weizmann Institute of Science, Israel) (Gao et al., 2018); PMCA2w/b, GCamP6s, CNTN4.2-Fc-His plasmids and AAV1.Syn.GCaMP6f.WPRE.SV40 (Addgene); shPMCA2 and scramble shRNA (VectorBuilder); and Fc-CNTNAP2$_{28–1261}$ (Rubio-Marrero *et al.*, 2016). Lentiviral vectors for expression of shPMCA or scramble were packaged, and titered by the Northwestern GET iN Core.

Biological process enrichment analysis—The gene annotation enrichment analysis tool DAVID v6.8 was used to perform biological process GO term enrichment (Huang da et al., 2009). For the secretome analysis, the previously published list of detected proteins (Kuhn *et al.*, 2016) was used as an initial dataset. For the hCSF analysis, we used data from CSF samples that had been subjected to high-speed ultracentrifugation to remove the potential contribution of extracellular vesicles to CSF composition (Chiasserini *et al.*, 2014). To determine the subset of proteins that undergo ectodomain shedding, we overlapped the datasets with proteins that are bound to the cell membrane (i.e., contain at least one transmembrane domain or a GPI anchor), based on UniProt annotations. To avoid any nomenclature discrepancies, all IDs were translated into *entrez* gene ID. Gene ontology (GO) analysis of the neuronal and hCSF sheddomes were background corrected

for all membrane anchored proteins to eliminate the possibility of skewing the data toward that group of proteins. For other analyses, we used *H. sapiens* as the background list. The $-\log_{10}$ of the Benjamini corrected *P*-value was calculated and graphed for the top five non-redundant GOTERM_BP_DIRECT categories, in which statistical significance is reached at a value of 1.3.

Disease enrichment analysis—A hypergeometric test was used to calculate the probability of finding an over-enrichment of disease-relevant genes in the secretome and hCSF gene ID lists and sub-lists (including membrane-anchored, and secreted proteins). As disease-relevant gene lists, we used all *de novo* gene lists from the supplementary data compiled in (Genovese et al., 2016), because *de novo* exonic mutations implicate individual genes with particular disorders. Only *de novo* variants affecting protein-coding regions or splice sites were included (e.g., missense, frameshift, and splice site mutations, altered stop codons, altered start codons, insertions, and deletions).

CSF-secretome correlation analysis—A list of proteins secreted from neurons in culture and their relative abundance (spectral counts) was obtained from data in published material (Kuhn et al., 2016). The list of secreted proteins was filtered to include proteins with a transmembrane domain or GPI anchor (defined by UniProt), producing a comprehensive list of putative ectodomain shedding in neurons, or the “neuronal sheddome.” A separate list of secreted soluble proteins (i.e., no transmembrane or GPI) was also produced. Similarly, two lists of proteins and their corresponding spectral counts were obtained from proteomic analysis of human CSF samples (Chiasserini et al., 2014), separating the group of membrane-anchored proteins defined by UniProt or “CSF sheddome” and the soluble proteins in the CSF. The correlation between CSF and neuronal sheddome proteins was analyzed with GraphPad Prism.

Protein-protein interaction network analysis—STRING v10.5 was used to perform protein-protein interaction (PPI) analysis. The PPI confidence is shown by the network edges, using experiments and databases as the active interaction sources, with medium confidence. We adjusted the network to fit four clusters and used the k means clustering method for creating the PPI network to provide a global and intuitive understanding of the functional properties of the proteins belonging to the synaptic sheddome, defined as the overlap between the hCSF dataset (610 IDs) and the PSD proteome (Bayes et al., 2012).

Separation of membrane and soluble fractions—We used a published protocol (Suzuki *et al.*, 2012) with slight modifications. One-month old male WT and *Cntnap2* KO mice were dissected. Cortices were homogenized with a dounce homogenizer in a Tris-based buffer (50 mM Tris-HCl, pH 7.6, 150 mM NaCl, and protease inhibitor cocktail, Sigma-Aldrich). The homogenates were centrifuged at 1,500×g for 10 min, and the supernatants were subsequently centrifuged at 100,000×g for 1 h. The pellet containing the membranes and the supernatants containing soluble proteins were analyzed by western blotting.

Neuronal cultures—High density (100,000 cells/cm^2) cortical neuron cultures were prepared from postnatal day zero (P0) *Cntnap2* WT or KO mice or Sprague-Dawley rat

E18 embryos as described previously (Srivastava et al., 2011). Briefly, neurons were plated onto coverslips coated with poly-D-lysine (0.2 mg/mL; Sigma-Aldrich), in feeding medium (neurobasal medium supplemented with B27 (Life Technologies), 0.5 mM glutamine, and penicillin/streptomycin). Four days later, 200 μM DL-APV (Abcam) was added to the medium. Half of the feeding medium+APV was replaced twice each week until the neurons were used.

Precipitation of extracellular media proteins—We centrifuged supernatants for 3 min at 16,000 rpm to eliminate suspended cells and other cell debris The supernatants were incubated with 0.015% deoxycholate for 5 min. Trichloroacetic acid (TCA, Sigma-Aldrich) was added to the supernatants to a final concentration of 20%. After an incubation period of 1 h, the samples were centrifuged at 18,000×g. The pellets were washed three times with ice-cold acetone. The remaining acetone was evaporated, and the pellets were dissolved in sample buffer.

Enzyme-Linked Immunosorbent Assay of hCSF—Unaffected controls and ASD postmortem hCSF samples were analyzed for CNTNAP2 concentration using the human CNTNAP2 Enzyme-Linked Imunosorbent Assay (ELISA) Kit (RayBiotech), according to the manufacturer's instructions. Human CNTNAP2 was used as a standard. To obtain measurements within the linear range of the standard curve, specimens of hCSF were diluted 200-fold.

Neuronal transfections—Cortical neurons were transfected at day *in vitro* (DIV) 21 using Lipofectamine 2000 (Thermo Fisher Scientific) following the manufacturer's recommendations, and the neurons were maintained in feeding media for 3 days after the transfection. Neurons were then fixed in 4% formaldehyde + 4% sucrose in PBS for 10 min and washed three times with PBS for 10 min. Coverslips were then processed for immunostaining. Only neurons that exhibited a pyramidal asymmetric morphology, with a single long apical and highly branching protrusion, and many basal shorter protrusions radiating from the soma, were selected for further analysis. Any signs of poor neuronal health excluded the cell from quantification.

Chemical LTP induction protocol—High density, DIV-24 rat cortical neurons were accommodated for 30 min in artificial (a) CSF (containing in mM: NaCl 125, KCl 2.5, $CaCl_2$ 2, $MgCl_2$ 1.25, glucose 11, $NaHCO_3$ 26.2, NaH_2PO_4 1, Hepes 10, and 200 μM APV, pH 7.4). Then, LTP was induced chemically by the application of a chemical cocktail containing 100 μM picrotoxin (Abcam), 1 μM strychnine (Abcam),10 μM glycine (Sigma-Aldrich), in 0 Mg^{2+}, 0 APV artificial cerebrospinal fluid (aCSF) for 30 min. After this, extracellular media proteins were collected and concentrated by the TCA method, and cells were lysed in RIPA buffer. When inhibitors or antagonists were employed, they were added in accommodation to the aCSF phase, as well as during the cLTP phase. The following chemicals were used: APV (200 μM, Abcam,) NBQX (10 μM, Tocris), TAPI-0 (25 μM, Enzo, which inhibits MMP13, MMP9, MMP1, TACE, and MMP3 with decreasing affinities (K_i in nM 0.2, 0.5, 6, 8.8, and 68, respectively)), GM6001 (50 μM, Sigma-Aldrich), and MMP9 inhibitor I (1 μM, Sigma-Aldrich).

Fractionation of neuronal homogenates—We followed a protocol described elsewhere, with slight modifications (Won et al., 2016). Briefly, 3-week-old rat cortical neurons were rinsed in PBS, and cells were collected in a PBS solution containing 1 mM $MgCl_2$, 0.1 mM $CaCl_2$, protease inhibitor cocktail (Sigma-Aldrich), and phosphatase inhibitor cocktail (Sigma-Aldrich). Cells were harvested after centrifugation at 16,000×g for 2 min, and lysed for 15 min in a hypotonic buffer (10 mM Tris, 1 mM $MgCl_2$, 0.1 mM $CaCl_2$, protease inhibitor cocktail, and phosphatase inhibitor cocktail, pH 7.5). Membranes were pelleted by centrifugation (20,000×g for 20 min) and lysed for 15 min in lysis buffer (PBS, 1 mM $MgCl_2$, 0.1 mM $CaCl_2$, 1% Triton-X-100, protease inhibitor cocktail, and phosphatase inhibitor cocktail). Then, samples were centrifuged at 20,000×g for 20 min, leaving the extrasynaptic fraction in the supernatant. The insoluble pellet containing the synaptic fraction was dissolved in PBS, 1 mM $MgCl_2$, 0.1 mM $CaCl_2$, 1% Triton X-100, and 1% SDS. Whole cell lysates and extrasynaptic and synaptic fractions were analyzed using western blotting.

Immunocytochemistry—On DIV-24, neurons were washed in PBS. For total staining, cells were fixed in 4% formaldehyde-4% sucrose-PBS for 10 min. Fixed neurons were permeabilized and blocked simultaneously (0.1% BSA, 4% NGS, 0.1% Triton-X-100 in PBS, 1 h at room temperature), followed by incubation of primary antibodies overnight at 4 °C. The coverslips were washed three times with PBS and incubated with the corresponding fluorophore-secondary antibodies (45 min, RT) (Alexa Fluor®488, Alexa Fluor®596, LifeTechnologies), as described previously. For surface staining, cells were fixed for 5 min in 4% formaldehyde-4% sucrose-PBS at RT, they were washed three times with PBS, and the surface antibody was incubated for 20 min at RT (in 0.1% BSA, 4% NGS, without Triton-X-100 in PBS). After that, cells were washed three times with PBS and they were permeabilized and blocked for 30 min at RT. Then, we followed the same steps as for total staining.

The coverslips were mounted onto slides using ProLong Antifade reagent (Invitrogen) and stored at 4 °C until the acquisition of the images. All images were acquired in the linear range of fluorescence intensity. When the vGLUT1 antibody was used, incubation with primary antibodies and the corresponding secondary antibodies was performed on 2 consecutive days to avoid cross-reaction of chicken Alexa Fluor®488 with guinea pig vGLUT1 primary antibody.

SIM imaging and analysis—3-week-old *Cntnap2* KO cortical neurons were transfected with GFP and an extracellularly tagged Flag-CNTNAP2. After a 30-min accommodation of the cells in aCSF (containing in mM: NaCl 125, KCl 2.5, $CaCl_2$ 2, $MgCl_2$ 1.25, glucose 11, $NaHCO_3$ 26.2, NaH_2PO_4 1, Hepes 10, pH 7.4), LTP was induced chemically with a cocktail containing 100 μM picrotoxin (Abcam), 1 μM strychnine (Abcam),10 μM glycine (Sigma-Aldrich), in 0 Mg^{2+}, 0 APV aCSF for 30 min. After this, cells were fixed and stained for GFP, vGLUT1, Flag, and CNTNAP2 C-terminal antibodies. Images were taken with an N-SIM microscope (100x, 1.49 N.A. objective) at the Nikon Imaging Center at Northwestern University, as previously described (Smith et al., 2014). Acquisition was set to 10 MHz, 14 bit with EM gain, and no binning. Autoexposure was kept at 100–300 ms, and the EM

gain multiplier restrained below 300. Laser power was adjusted to keep lookup tables within the first quarter of the scale. Reconstruction parameters Illumination Modulation Contrast, High Resolution Noise Suppression, and Out of Focus Blur Suppression (0.96, 1.19, and 0.17, respectively) were kept consistent across experiments and imaging sessions. Images were analyzed with ImageJ. For the experiments stained for GFP, CNTNAP2 N-term and vGLUT1 (Fig.5A–C), GFP ROIs were generated and expanded by 5 μm and this area was removed from each channel to select "non-GFP" ROIs within the nearby, non-transfected neurons. ROIs and the overlap between indicated proteins were generated to give the number and area of puncta and overlapping puncta. Image averages were normalized to the experimental average to reduce the impact of biological variability. For the experiments stained for GFP, Flag, CNTNAP2 C-term and vGLUT1 (Fig. 5D–F), CNTNAP2-ecto was identified using the AND, OR, and XOR functions, to identify signals that contained only the Flag staining (N-terminal or extracellular) with no C-terminal/intracellular signal. This Flag signal, void of CNTNAP2 C-terminal signal, was considered to correspond to CNTNAP2-ecto and was analyzed in two different compartments: GFP or overlap between GFP and vGLUT1 (synaptic). The area occupied by CNTNAP2-ecto and the number of puncta were measured within the GFP and synaptic regions. 3D reconstructions were performed with Imaris Viewer.

Electroconvulsive shock and CSF extraction—2–3-month-old male Sprague-Dawley rats were surgically implanted with skull screws insulated with dental cement (Burgdorf et al., 2019). At least 2 weeks after the implantation, a 30-second electrical stimulation was administered via a master 8 stimulator and stimulus isolation unit (AMPI). This electrical stimulation consisted of trains (6 per second) of five 1 mA pulses (0.1 ms in duration, 10 ms interstimulus interval, 50 ms total pulse duration). The positive pole was placed at the medial prefrontal cortex and the negative pole at the cerebellum. Four or eight hours after stimulation, animals were anesthetized with isoflurane and cerebrospinal fluid was drawn from the cisterna magna via a 27-gauge winged infusion set (Terumo) following a slightly modified protocol described elsewhere (Lim et al., 2018).

CNTNAP2-ecto protein production—CNTNAP2-ecto obtained following this protocol was used for data in Fig. 6 and Fig. S5. HEK cells were plated in PDL-coated, 10-cm^2 dishes and transfected with Flag-CNTNAP2 using Lipofectamine 2000 (Thermo Fisher) following the manufacturer's recommendations. After a 2-day transfection, supernatants from CNTNAP2-transfected and non-transfected cultures were collected, centrifuged at 700×g, and filtered through a 0.22-μm filter. To concentrate the supernatants to a manageable volume, samples were spin-filtered with 50 kDa molecular cut-off filters (MilliporeSigma). The concentrated supernatant was then affinity-purified with anti-Flag M2 affinity beads (Sigma-Aldrich) following the manufacturer's instructions. Briefly, beads were washed and rinsed, added to the concentrated supernatants, and rocked at 4 °C for 4 h. After a 2-min centrifugation at 2,000×g, the beads were rinsed three times with TBS, and the proteins were eluted with 100 mM Gly, pH 3.5. The beads were removed by centrifugation. To neutralize the solution, 1 M Tris, pH 8.5, was added to the eluate. Finally, the samples containing the purified CNTNAP2-ecto and the vehicle control were dialyzed three times

using 0.5 mL100 kDa spin filters (MilliporeSigma) to remove the glycine and substitute a TBS solution.

Affinity chromatography and mass spectrometry

Tissue preparation.: Cortices from 20 6–8-week-old male C57BL6J mice were homogenized on ice with a dounce homogenizer in buffer HB (20 mM Hepes, pH 7.4, 320 mM sucrose, 5 mM EDTA, protease inhibitors). Homogenates were centrifuged at 3,000×g for 15 min at 4 °C to remove nuclei and cell debris. The supernatant was further centrifuged at 38,400×g (15 min, 4 °C) and the pellet was resuspended in buffer SB1 (20 mM Hepes, pH 7.4, 1 M KI, 5 mM EDTA, protease inhibitors) to remove peripheral proteins. This homogenate was centrifuged at 38,400×g (15 min, 4 °C) to collect membranes. Pellet-containing membranes were washed with buffer SB2 (20 mM Hepes, pH 7.4, 5 mM EDTA, protease inhibitors) to remove KI, and the homogenate was centrifuged again at 38,400×g for 30 min at 4 °C. The pellet was then resuspended in buffer RB (20 mM Hepes, pH 7.4, 100 mM NaCl, 5 mM EDTA, 5 mM EGTA, 1% CHAPS, protease inhibitors) and rotated for 1.5h at 4 °C to solubilize the membranes. Finally, the homogenate was ultracentrifuged at 100,000×g for 1 h at 4 °C to remove insoluble materials. The final supernatant was split in halves. Vehicle or CNTNAP2-ecto was added to the membrane homogenate and incubated overnight at 4 °C. The following morning, the same amount of Flag-agarose beads (Sigma-Aldrich) was added to each sample and incubated with rotation for 1.5 h at 4 °C. After capture, samples were centrifuged at 2,000×g for 1 min, and the beads were rinsed with buffer RB three times. The samples containing the beads were passed through disposable chromatography columns (BioRad); then bait and prey proteins were eluted by adding a solution containing 100 mM glycine, 1% CHAPS, pH 2.5, three times. The eluate was precipitated by adding trichloracetic acid to a final concentration of 20% over 1 h at 4 °C, and the solution was then centrifuged at 18,000×g for 1 h at 4 °C. Finally, the pellet was washed three times with ice cold acetone, and the samples were kept at RT to dry. They were stored at −80 °C until they were analyzed by mass spectrometry. *Sample preparation for LC-MS/MS analysis.* We followed a protocol described elsewhere (Hickox et al., 2017). The precipitated protein pellets were solubilized in 100 μL of 8 M urea for 30 min; 100 μL of 0.2% ProteaseMAX (Promega) was then added, and the mixture was incubated for an additional 2 h. The protein extracts were reduced and alkylated as described previously (Chen et al., 2008), followed by the addition of 300 μL of 50 mM ammonium bicarbonate, 5 μL of 1% ProteaseMAX, and 2 μg of sequence-grade trypsin (Promega). Samples were digested overnight in a 37 °C thermomixer (Eppendorf). For Orbitrap Fusion Tribrid MS analysis, the tryptic peptides were purified with Pierce C18 spin columns and fractionated with increasing acetonitrile (ACN) concentrations (30% and 70%). Up to 3 μg of each fraction was auto-sampler loaded with a Thermo Fisher EASY nLC 1000 or nLC 1200 UPLC pump onto a vented Acclaim Pepmap 100, 75 μm by 2 cm, nanoViper trap column coupled to a nanoViper analytical column (Thermo Fisher 164570, 3 μm, 100 Å, C18, 0.075 mm, 500 mm) with a stainless steel emitter tip assembled on the Nanospray Flex Ion Source with a spray voltage of 2,000 V. Buffer A contained 94.875% H_2O with 5% ACN and 0.125% formic acid (FA), and buffer B contained 99.875% ACN with 0.125% FA. The chromatographic run was 4 h in total with the following buffer B profile: 0–7% for 7 min, 10% for 6 min, 25% for 160 min, 33% for 40 min, 50% for 7 min, 95% for 5 min, and 95%

again for 15 min. Additional MS parameters include: ion transfer tube temp=300 °C, Easy-IC internal mass calibration, default charge state=2, and cycle time=3 s. The detector type was set to Orbitrap, with 60 K resolution, wide quad isolation, mass range=normal, scan range=300–1500 m/z, max injection time=50 ms, AGC target=200,000, microscans=1, S-lens RF level=60, without source fragmentation, and datatype=positive and centroid. MIPS was set to 'on', and included charge states=2–6 (reject unassigned). Dynamic exclusion was enabled, with n=1 for 30 and 45 s exclusion duration at 10 ppm for high and low, respectively. Precursor selection decision=most intense, top 20, isolation window=1.6, scan range=auto normal, first mass=110, collision energy 30%, CID, Detector type=ion trap, Orbitrap resolution=30K, IT scan rate=rapid, max injection time=75 ms, AGCtarget=10,000, Q=0.25, inject ions for all available parallelizable time. *Tandem mass spectra analysis.* Peptide spectral files from pooled samples or from biological replicates were combined for database searching. Raw spectrum files were extracted into MS1 and MS2 files using the in-house program RawXtractor or RawConverter (http://fields.scripps.edu/downloads.php) (He et al., 2015) and the tandem mass spectra were searched against UniProt's mouse protein database (downloaded on 09-21-2015; UniProt Consortium, 2015) and matched to sequences using the ProLuCID/SEQUEST algorithm (ProLuCID version 3.1) (Eng et al., 1994) with 50 ppm peptide mass tolerance for precursor ions and 600 ppm for fragment ions. The human CNTNAP2 amino acid sequence was manually added to the database.

The search space included all fully and half-tryptic or non-tryptic (for CNTNAP2 sequence mapping) peptide candidates that fell within the mass tolerance window with no miscleavage constraint. Peptides were assembled and filtered with DTASelect2 (version 2.1.3) (Cociorva et al., 2007; Tabb et al., 2002) through Integrated Proteomics Pipeline (IP2 version 3, Integrated Proteomics Applications). To estimate peptide probabilities and false discovery rates (FDR) accurately, we used a target/decoy database containing the reversed sequences of all the proteins appended to the target database (Peng et al., 2003). Each protein identified was required to have a minimum of one peptide of minimal length of six amino acid residues; however, this peptide had to be an excellent match with a FDR <0.001. After the peptide/spectrum matches were filtered, we estimated that the protein FDRs were ≤1% for each sample analysis. Resulting protein lists included subset proteins to allow for consideration of all possible protein forms implicated by a given peptide identified from the complex protein mixtures. The fold enrichment of each prey protein shown in Fig. 4C was calculated by subtracting the number of spectral counts in the sample containing the bait minus the sample containing the vehicle control. This value was then divided by the total number of spectral counts obtained for CNTNAP2-ecto.

Expression and purification of CNTNAP2-ecto—The CNTNAP2-ecto produced and purified by the method explained here was employed in experiments Fig. 7, 8, S6, and S8. The construct encoding the entire extracellular domain of CNTNAP2 from residue 28 to 1261 was fused to the Fc portion of human IgG1 (Fc-CNTNAP2$_{28–1261}$) as detailed elsewhere (Rubio-Marrero *et al.*, 2016). This construct was transfected into HEK293GnTI- cells and the cells were selected by growth in the antibiotic G418. For large-scale protein expression, stable cells were maintained at 37 °C and 5% (v/v) CO_2 in DMEM containing up to 5% (v/v) FBS. CNTNAP2-Fc secreted in the medium was affinity purified using

CaptivA ® Protein A Affinity Resin (RepliGen) and subsequently cleaved with recombinant 3C protease to remove the Fc fragment and leave the mature (i.e., no leader peptide) extracellular domain of CNTNAP2. The purified protein was buffer exchanged into 10 mM Hepes, pH 7.4, and 150 mM NaCl, concentrated to ~3 to ~6 mg/mL, and stored at −80 °C until used for experiments.

Endogenous immunoprecipitation of PMCA2—Two 8-week-old mouse cortices were homogenized in a sucrose buffer (20 mM HEPES pH 7.4, 320 mM sucrose, 5 mM EDTA with Roche protease inhibitor cocktail) and centrifuged at 3,000×g for 20 min at 4 °C. The collected supernatant was centrifuged further at 16,000×g for 30 min at 4 °C to obtain a membrane pellet. Pellets were then resuspended with binding buffer (50 mM HEPES pH 7.5, 1% triton-X-100, 150 mM NaCl, 1 mM EDTA with protease inhibitor cocktail) and solubilized for 1 h at 4 °C with rotation. Proteins were immunoprecipitated overnight with 3 μg of PMCA2 antibody or IgG as a control at 4 °C, followed by 1 h incubation with protein A/G agarose beads (Thermo Fisher). The complexes were washed three times. Samples were then denatured (5 min, 95 °C). The immunoprecipitated proteins were separated with a 10% SDS-PAGE and bands were detected by western blotting.

Cytosolic Ca^{2+} imaging in HEK293 cells—One day after seeding, cells were transfected with GFP-PMCA2w/b. After 2 days, cells were loaded with 1 μM Fura-2AM (Life Technologies), a fluorescent Ca^{2+} indicator used to measure cytosolic free Ca^{2+} levels. Cells were rinsed twice with recording solution containing, in mM, NaCl 145, KCl 5, $CaCl_2$ 2, $MgCl_2$ 1, glucose 10, and Hepes 10, pH 7.4. The glass-bottom dish containing the cells was placed on the stage of a C2 Nikon microscope where the temperature was maintained at 37 °C. Images were acquired using a 20X objective. After 60 s of basal recording, the cells were treated with either vehicle or CNTNAP2-ecto, after which 0.5 mM ATP (Sigma-Aldrich) was added to elicit a cytosolic Ca^{2+} signal. Acquired images were analyzed with NIS Elements (Nikon), selecting both PMCA2 transfected and non-transfected cells.

Ca^{2+} imaging in dissociated neurons—At day-in-culture 17, rat cortical neurons were transfected with the cytosolic genetic Ca^{2+} indicator GCaMP6s and the red cell fill DsRed Express2. After 2 days, cells were rinsed twice with aCSF containing (in mM) NaCl 125, KCl 2.5, $CaCl_2$ 2, $MgCl_2$ 1.25, glucose 11, $NaHCO_3$ 26.2, NaH_2PO_4 1, and Hepes 10, pH 7.4. After 60 s of basal recording, the cells were treated with either vehicle or CNTNAP2-ecto for 5 min, after which 30 mM KCl was added to elicit a cytosolic Ca^{2+} signal. Acquired images were analyzed with NIS elements (Nikon). For the analysis of Ca^{2+} in soma, a C2 Nikon microscope and a 20X objective were used. The glass-bottom dish containing the neurons was placed on the stage of the microscope where the temperature was maintained at 37 °C. For Ca^{2+} imaging in dendrites and spines, neurons were plated in glass coverslips that were placed at 37 °C in a metallic insert on the stage of a Nikon A1R+ Confocal Laser Microscope System equipped with resonant scanning technology, GaAsp detectors and a 100X objective. To allow for the fastest Ca^{2+} imaging, only a section of a dendrite with spines was imaged. Then maximal projections were obtained for the final analysis.

Ca^{2+} imaging in PMCA2 knockdown neurons—For analysis of the role of PMCA2 on CNTNAP2-ecto's effect on Ca^{2+} extrusion, neurons were infected 1 week before imaging with the genetic Ca^{2+} indicator AAV1.Syn.GCaMP6f.WPRE.SV40 (Brennaman et al., 2014; Chen et al., 2013). Three days before imaging, neurons were transfected with a plasmid expressing an shRNA against PMCA2 or a scrambled control. Cells were then treated with CNTNAP2-ecto or a boiled CNTNAP2-ecto control for 5 min, after which 30 mM KCl was added to the recording solution to induce a Ca^{2+} signal. A C2 Nikon microscope and a 20X objective were used for imaging. The temperature was maintained at 37 °C during imaging.

Ca^{2+} imaging in brain slices—P5-P7 male C57BL6J mice were deeply anesthetized with 5% isoflurane in O_2 and decapitated. The brain was rapidly extracted and placed on ice-cold modified aCSF containing (in mM) NaCl 125, $NaHCO_3$ 26, glucose 11, KCl 2.5, NaH_2PO_4 1.25, $CaCl_2$ 2.5, $MgCl_2$ 6, and kynurenic acid 1 for 2–3 min and then glued on a vibratome VT1000S (Leica). The slicing chamber was filled with the same ice-cold aCSF. Slices then recovered at 34 °C for at least 45 min in aCSF (in mM, NaCl 125, $NaHCO_3$ 26, glucose 11, KCl 2.5, NaH_2PO_4 1.25, $CaCl_2$ 2.5, $MgCl_2$ 1.3) before incubation with the Ca^{2+} sensor Cal520-AM (15 mM, AAT Bioquest) and the glial indicator SR-101 (1 μM, Sigma-Aldrich) for 45 min at 34 °C with constant bubbling of 95% O_2/5% CO_2 in a custom-made incubator. Slices were then pre-incubated for 1 h with 10 nM of the CNTNAP2-ecto or vehicle at 34 °C before imaging. Slices were transferred to an imaging chamber (Warner) with a constant flow of 3 mL/min of 95% O_2/5% CO_2 in aCSF under a Nikon A1R multiphoton microscope, immersion objective 25X, NA 1.1. A chameleon laser was tuned at 820 nm and the power was set at 12–16 mW. aCSF was kept at 37.5 °C by a heated controller (TC344, Warner Instrument) to have a final temperature of 32–33 °C in the imaged sample. Slices were allowed to stabilize for 5 min in the chamber before recording. Responses evoked by 30 mM KCl were acquired at 2 frames/s, and spontaneous activity was recorded at a speed of 3 frames/s with 7.5 mM of KCl to induce spontaneous network events (Feldt Muldoon et al., 2013).

Spontaneous activity and synchrony analysis—Regions of interest were traced manually on somas based on the maximum projection obtained in ImageJ, with the investigator blinded to the experimental conditions. Somas stained for the red glial dye SR-101 were not included in the analysis. The background was subtracted, and the mean intensity was used as the intensity of the fluorescence for each time point. The normalized data were analyzed in Matlab (Math Works) using a routine developed by us based on the "findpeak" functions of the software. The minimum variation of intensity was set at 6% for neuronal cultures and at 10% for slices. Regions of interest presenting no transients (Ca^{2+} spikes) during the time course of the movie were discarded from the analysis. To prevent bias while detecting the time windows when the neuronal network was synchronized, we used a method based on 10,000 random permutations over time of the binary Ca^{2+} transients for each neuron (Fig. S8A–E). The generated distribution of the number of events per frame is used to determine a threshold of significant synchrony corresponding to $Threshold\ Synchrony = \mu + 3\ \sigma$ where μ is the average number of events per frame in the 10,000 shuffled events, and σ is the standard deviation of number of events per frame in the

shuffled data. The fraction of synchronized transients is calculated by dividing the number of synchronized transients by the total number of events for each individual neuron.

Contactin-4 expression and purification—CNTN4.2-Fc-His plasmid (Addgene) was transfected into eight 10-cm^2 plates of HEK293T cells using Lipofectamine 2000 (Thermo Fisher) in accordance with the manufacturer's instructions. Cells were incubated for 4 days in serum-free OptiMEM (Thermo Fisher), before the medium was collected. The medium was centrifuged at 1000×g for 5 min to remove cellular debris. Next, 25 mL of the medium was incubated with 0.5 mL prewashed protein A/G agarose beads (Thermo Fisher) overnight at 4 °C. Beads were washed in 5 mL PBS, then collected by centrifugation at 1000xg for 5 min. The supernatant was discarded. Contactin4-FC was eluted in 100 mM Glycine, pH2.5 and 500 mM NaCl. The eluted sample was applied to a 50 kDa MWCO PES centrifugal concentrator (Sigma-Aldrich) for buffer exchange to PBS, and concentration to 0.5 mL. Protein concentration was calculated by A_{280} and analytical SDS-PAGE and assessed to be >90% pure. Finally, 20 μL aliquots were prepared and flash frozen in liquid nitrogen before long-term storage at −80 °C.

Multielectrode Array Analysis—For multielectrode array (MEA) studies, 48-well MEA plates with 16 electrodes per well (Axion Biosystems) were coated overnight with PDL. Primary cortical neurons were seeded in a 10 μL drop of Neurobasal medium at the center of each well at a density of 95,000 cells/well, and then covered with 250 μL Neurobasal medium after 30 min in the incubator. Twice each week, half of the media was replaced with feeding medium. At 3 weeks-*in-vitro*, the culturing medium was switched to aCSF containing either vehicle, CNTNAP2-ecto or boiled CNTNAP2-ecto, and incubated at 37 °C for 45 min. Due to changes in electrical activity caused by physical movement of the MEA, each plate was placed in the Maestro instrument for 10 min for acclimatization and then real-time activity was recorded for an additional 10 min using the AxIS 2.5 software. All recordings were conducted at 37 °C in 5% CO_2. A bandpass filter (200 Hz to 3 kHz) was applied. Spikes were detected using a threshold of ±6 times the standard deviation of the noise on each electrode. We analyzed multielectrode data using the Axion Biosystems Neural Metrics Tool, and electrodes active if at least 5 spikes/min were detected. Single electrode bursts were identified as a minimum of five spikes with a maximum interspike interval (ISImax) of 100 milliseconds. Network bursts were identified as a minimum of 10 spikes, with an ISImax of 100 milliseconds, covered by at least 25% of electrodes in each well (Fruscione et al., 2018). The synchrony index was computed through AxIS software. We used six independent cultures for MEA recordings. All data in Fig. 8L–M and Fig. S8J–L reflects well-wide averages, with the number of wells per condition represented by n values. To compensate for biological variability between cultures, data was normalized to 100% to the scramble vehicle conditions.

QUANTIFICATION AND STATISTICAL ANALYSIS

Statistical analysis was performed using GraphPad Prism (GraphPad Software Inc.). To compare differences between two groups, a Student's *t*-test was used for a Gaussian distribution of data, while a Mann Whitney test was used for a non-Gaussian distribution. To compare multiple variables, two-way ANOVA followed by a *post hoc* test (Gaussian

distribution of data) or Kruskal-Wallis followed by a *post hoc* test (non-Gaussian distribution of data) were used. When the *post hoc* test was used, it is specified in the figure legends. Data distribution was considered Gaussian after passing the Kolmogorov-Smirnov test or the F-test to compare variances when n<5. Statistical significance was defined as $P<0.05$. All statistical tests used were two-sided.

Supplementary Material

Refer to Web version on PubMed Central for supplementary material.

ACKNOWLEDGMENTS

This work was supported by grant MH097216 from the US National Institute of Mental Health (to P.P.), by an individual Biomedical Research Award from the Martwell Foundation (to J.N.S), by National Institutes of Health (NIH) grant R01-MH092906 (to D.C.), and by the New Jersey Commission on Traumatic Brain Injury Research (CBIR16PIL035, to D.C.), and the Fred & Santa Barile Children's Medical Research Trust (to D.C.). SIM imaging work was performed at the Northwestern University Center for Advanced Microscopy, generously supported by National Cancer Institute grant CCSG-P30-CA060553. The Nikon N-SIM system was purchased through the support of NIH grant 1S10OD016342-01. We thank Drs. Constadina Arvanitis and David Kirchenbüchler for help with SIM imaging and live Ca^{2+} imaging. Human CSF was obtained from the NIH Neurobiobank at the University of Maryland, Baltimore (MD).

REFERENCES

Alford ST, and Alpert MH (2014). A synaptic mechanism for network synchrony. Front Cell Neurosci 8, 290. 10.3389/fncel.2014.00290. [PubMed: 25278839]

Altmeppen HC, Prox J, Krasemann S, Puig B, Kruszewski K, Dohler F, Bernreuther C, Hoxha A, Linsenmeier L, Sikorska B, et al. (2015). The sheddase ADAM10 is a potent modulator of prion disease. Elife 4. 10.7554/eLife.04260.

Bakkaloglu B, O'Roak BJ, Louvi A, Gupta AR, Abelson JF, Morgan TM, Chawarska K, Klin A, Ercan-Sencicek AG, Stillman AA, et al. (2008). Molecular cytogenetic analysis and resequencing of contactin associated protein-like 2 in autism spectrum disorders. Am J Hum Genet 82, 165–173. 10.1016/j.ajhg.2007.09.017. [PubMed: 18179895]

Bayes A, Collins MO, Croning MD, van de Lagemaat LN, Choudhary JS, and Grant SG (2012). Comparative study of human and mouse postsynaptic proteomes finds high compositional conservation and abundance differences for key synaptic proteins. PLoS One 7, e46683. 10.1371/journal.pone.0046683. [PubMed: 23071613]

Bereczki E, Bogstedt A, Hoglund K, Tsitsi P, Brodin L, Ballard C, Svenningsson P, and Aarsland D (2017). Synaptic proteins in CSF relate to Parkinson's disease stage markers. NPJ Parkinsons Dis 3, 7. 10.1038/s41531-017-0008-2. [PubMed: 28649607]

Brennaman LH, Moss ML, and Maness PF (2014). EphrinA/EphA-induced ectodomain shedding of neural cell adhesion molecule regulates growth cone repulsion through ADAM10 metalloprotease. J Neurochem 128, 267–279. 10.1111/jnc.12468. [PubMed: 24117969]

Brini M, and Carafoli E (2009). Calcium pumps in health and disease. Physiol Rev 89, 1341–1378. 10.1152/physrev.00032.2008. [PubMed: 19789383]

Burette A, and Weinberg RJ (2007). Perisynaptic organization of plasma membrane calcium pumps in cerebellar cortex. J Comp Neurol 500, 1127–1135. 10.1002/cne.21237. [PubMed: 17183553]

Burgdorf JS, Christian EP, Sørensen L, Stanton PK, Leaderbrand K, Madsen TM, Khan MA, Kroes RA, and Moskal JR (2019). A translational EEG-based approach to assess modulation of long-lasting NMDAR-dependent synaptic plasticity. Psychopharmacology (Berl) 236, 3687–3693. 10.1007/s00213-019-05341-w. [PubMed: 31392357]

Chen EI, McClatchy D, Park SK, and Yates Iii JR (2008). Comparisons of Mass Spectrometry Compatible Surfactants for Global Analysis of the Mammalian Brain Proteome. Analytical Chemistry 80, 8694–8701. 10.1021/ac800606w. [PubMed: 18937422]

Chen TW, Wardill TJ, Sun Y, Pulver SR, Renninger SL, Baohan A, Schreiter ER, Kerr RA, Orger MB, Jayaraman V, et al. (2013). Ultrasensitive fluorescent proteins for imaging neuronal activity. Nature 499, 295–300. 10.1038/nature12354. [PubMed: 23868258]

Chiasserini D, van Weering JR, Piersma SR, Pham TV, Malekzadeh A, Teunissen CE, de Wit H, and Jimenez CR (2014). Proteomic analysis of cerebrospinal fluid extracellular vesicles: a comprehensive dataset. J Proteomics 106, 191–204. 10.1016/j.jprot.2014.04.028. [PubMed: 24769233]

Cociorva D, D LT, and Yates JR (2007). Validation of tandem mass spectrometry database search results using DTASelect. Curr Protoc Bioinformatics Chapter 13, Unit 13 14. 10.1002/0471250953.bi1304s16.

Collins MA, An J, Hood BL, Conrads TP, and Bowser RP (2015). Label-Free LC-MS/MS Proteomic Analysis of Cerebrospinal Fluid Identifies Protein/Pathway Alterations and Candidate Biomarkers for Amyotrophic Lateral Sclerosis. J Proteome Res 14, 4486–4501. 10.1021/acs.jproteome.5b00804. [PubMed: 26401960]

Conant K, Allen M, and Lim ST (2015). Activity dependent CAM cleavage and neurotransmission. Front Cell Neurosci 9, 305. 10.3389/fncel.2015.00305. [PubMed: 26321910]

Duits FH, Brinkmalm G, Teunissen CE, Brinkmalm A, Scheltens P, Van der Flier WM, Zetterberg H, and Blennow K (2018). Synaptic proteins in CSF as potential novel biomarkers for prognosis in prodromal Alzheimer's disease. Alzheimers Res Ther 10, 5. 10.1186/s13195-017-0335-x. [PubMed: 29370833]

Eng JK, McCormack AL, and Yates JR (1994). An approach to correlate tandem mass spectral data of peptides with amino acid sequences in a protein database. J Am Soc Mass Spectrom 5, 976–989. 10.1016/1044-0305(94)80016-2. [PubMed: 24226387]

Feldt Muldoon S, Soltesz I, and Cossart R (2013). Spatially clustered neuronal assemblies comprise the microstructure of synchrony in chronically epileptic networks. Proc Natl Acad Sci U S A 110, 3567–3572. 10.1073/pnas.1216958110. [PubMed: 23401510]

Fruscione F, Valente P, Sterlini B, Romei A, Baldassari S, Fadda M, Prestigio C, Giansante G, Sartorelli J, Rossi P, et al. (2018). PRRT2 controls neuronal excitability by negatively modulating Na+ channel 1.2/1.6 activity. Brain 141, 1000–1016. 10.1093/brain/awy051. [PubMed: 29554219]

Gao R, Piguel NH, Melendez-Zaidi AE, Martin-de-Saavedra MD, Yoon S, Forrest MP, Myczek K, Zhang G, Russell TA, Csernansky JG, et al. (2018). CNTNAP2 stabilizes interneuron dendritic arbors through CASK. Molecular Psychiatry 23, 1832–1850. 10.1038/s41380-018-0027-3. [PubMed: 29610457]

Genovese G, Fromer M, Stahl EA, Ruderfer DM, Chambert K, Landen M, Moran JL, Purcell SM, Sklar P, Sullivan PF, et al. (2016). Increased burden of ultra-rare protein-altering variants among 4,877 individuals with schizophrenia. Nat Neurosci 19, 1433–1441. 10.1038/nn.4402. [PubMed: 27694994]

Grell M, Douni E, Wajant H, Lohden M, Clauss M, Maxeiner B, Georgopoulos S, Lesslauer W, Kollias G, Pfizenmaier K, and Scheurich P (1995). The transmembrane form of tumor necrosis factor is the prime activating ligand of the 80 kDa tumor necrosis factor receptor. Cell 83, 793–802. [PubMed: 8521496]

Haass C, Kaether C, Thinakaran G, and Sisodia S (2012). Trafficking and proteolytic processing of APP. Cold Spring Harb Perspect Med 2, a006270. 10.1101/cshperspect.a006270. [PubMed: 22553493]

He L, Diedrich J, Chu YY, and Yates JR 3rd (2015). Extracting Accurate Precursor Information for Tandem Mass Spectra by RawConverter. Anal Chem 87, 11361–11367. 10.1021/acs.analchem.5b02721. [PubMed: 26499134]

Hickox AE, Wong AC, Pak K, Strojny C, Ramirez M, Yates JR 3rd, Ryan AF, and Savas JN (2017). Global Analysis of Protein Expression of Inner Ear Hair Cells. J Neurosci 37, 1320–1339. 10.1523/JNEUROSCI.2267-16.2016. [PubMed: 28039372]

Huang da W, Sherman BT, and Lempicki RA (2009). Systematic and integrative analysis of large gene lists using DAVID bioinformatics resources. Nat Protoc 4, 44–57. 10.1038/nprot.2008.211. [PubMed: 19131956]

Iida S, Shimba K, Sakai K, Kotani K, and Jimbo Y (2018). Synchronous firing patterns of induced pluripotent stem cell-derived cortical neurons depend on the network structure consisting of excitatory and inhibitory neurons. Biochem Biophys Res Commun 501, 152–157. 10.1016/j.bbrc.2018.04.197. [PubMed: 29723524]

Jiao SS, Bu XL, Liu YH, Wang QH, Liu CH, Yao XQ, Zhou XF, and Wang YJ (2015). Differential levels of p75NTR ectodomain in CSF and blood in patients with Alzheimer's disease: a novel diagnostic marker. Transl Psychiatry 5, e650. 10.1038/tp.2015.146. [PubMed: 26440538]

Kester MI, Teunissen CE, Crimmins DL, Herries EM, Ladenson JH, Scheltens P, van der Flier WM, Morris JC, Holtzman DM, and Fagan AM (2015). Neurogranin as a Cerebrospinal Fluid Biomarker for Synaptic Loss in Symptomatic Alzheimer Disease. JAMA Neurol 72, 1275–1280. 10.1001/jamaneurol.2015.1867. [PubMed: 26366630]

Khoonsari PE, Haggmark A, Lonnberg M, Mikus M, Kilander L, Lannfelt L, Bergquist J, Ingelsson M, Nilsson P, Kultima K, and Shevchenko G (2016). Analysis of the Cerebrospinal Fluid Proteome in Alzheimer's Disease. PLoS One 11, e0150672. 10.1371/journal.pone.0150672. [PubMed: 26950848]

Kuhn PH, Colombo AV, Schusser B, Dreymueller D, Wetzel S, Schepers U, Herber J, Ludwig A, Kremmer E, Montag D, et al. (2016). Systematic substrate identification indicates a central role for the metalloprotease ADAM10 in axon targeting and synapse function. Elife 5. 10.7554/eLife.12748.

Kuhn PH, Koroniak K, Hogl S, Colombo A, Zeitschel U, Willem M, Volbracht C, Schepers U, Imhof A, Hoffmeister A, et al. (2012). Secretome protein enrichment identifies physiological BACE1 protease substrates in neurons. EMBO J 31, 3157–3168. 10.1038/emboj.2012.173. [PubMed: 22728825]

Lavi A, Perez O, and Ashery U (2015). Shaping Neuronal Network Activity by Presynaptic Mechanisms. PLoS Comput Biol 11, e1004438. 10.1371/journal.pcbi.1004438. [PubMed: 26372048]

Lavi A, Sheinin A, Shapira R, Zelmanoff D, and Ashery U (2014). DOC2B and Munc13–1 differentially regulate neuronal network activity. Cereb Cortex 24, 2309–2323. 10.1093/cercor/bht081. [PubMed: 23537531]

Lichtenthaler SF, Lemberg MK, and Fluhrer R (2018). Proteolytic ectodomain shedding of membrane proteins in mammals-hardware, concepts, and recent developments. EMBO J 37. 10.15252/embj.201899456.

Lim NK, Moestrup V, Zhang X, Wang WA, Moller A, and Huang FD (2018). An Improved Method for Collection of Cerebrospinal Fluid from Anesthetized Mice. Journal of visualized experiments : JoVE. 10.3791/56774.

Lim ST, Chang A, Giuliano RE, and Federoff HJ (2012). Ectodomain shedding of nectin-1 regulates the maintenance of dendritic spine density. J Neurochem 120, 741–751. 10.1111/j.1471-4159.2011.07592.x. [PubMed: 22118475]

Macron C, Lane L, Nunez Galindo A, and Dayon L (2018). Deep Dive on the Proteome of Human Cerebrospinal Fluid: A Valuable Data Resource for Biomarker Discovery and Missing Protein Identification. J Proteome Res 17, 4113–4126. 10.1021/acs.jproteome.8b00300. [PubMed: 30124047]

Mathalon DH, and Sohal VS (2015). Neural Oscillations and Synchrony in Brain Dysfunction and Neuropsychiatric Disorders: It's About Time. JAMA Psychiatry 72, 840–844. 10.1001/jamapsychiatry.2015.0483. [PubMed: 26039190]

McCormick DA, and Contreras D (2001). On the cellular and network bases of epileptic seizures. Annu Rev Physiol 63, 815–846. 10.1146/annurev.physiol.63.1.815. [PubMed: 11181977]

McIlwain DR, Lang PA, Maretzky T, Hamada K, Ohishi K, Maney SK, Berger T, Murthy A, Duncan G, Xu HC, et al. (2012). iRhom2 regulation of TACE controls TNF-mediated protection against Listeria and responses to LPS. Science 335, 229–232. 10.1126/science.1214448. [PubMed: 22246778]

Nagappan-Chettiar S, Johnson-Venkatesh EM, and Umemori H (2017). Activity-dependent proteolytic cleavage of cell adhesion molecules regulates excitatory synaptic development and function. Neurosci Res 116, 60–69. 10.1016/j.neures.2016.12.003. [PubMed: 27965136]

Nagy V, Bozdagi O, Matynia A, Balcerzyk M, Okulski P, Dzwonek J, Costa RM, Silva AJ, Kaczmarek L, and Huntley GW (2006). Matrix metalloproteinase-9 is required for hippocampal late-phase long-term potentiation and memory. J Neurosci 26, 1923–1934. 10.1523/JNEUROSCI.4359-05.2006. [PubMed: 16481424]

Niggli V, Adunyah ES, and Carafoli E (1981). Acidic phospholipids, unsaturated fatty acids, and limited proteolysis mimic the effect of calmodulin on the purified erythrocyte Ca2+ - ATPase. J Biol Chem 256, 8588–8592. [PubMed: 6455424]

Panzeri S, Macke JH, Gross J, and Kayser C (2015). Neural population coding: combining insights from microscopic and mass signals. Trends in cognitive sciences 19, 162–172. 10.1016/j.tics.2015.01.002. [PubMed: 25670005]

Peixoto RT, Kunz PA, Kwon H, Mabb AM, Sabatini BL, Philpot BD, and Ehlers MD (2012). Transsynaptic signaling by activity-dependent cleavage of neuroligin-1. Neuron 76, 396–409. 10.1016/j.neuron.2012.07.006. [PubMed: 23083741]

Penagarikano O, Abrahams BS, Herman EI, Winden KD, Gdalyahu A, Dong H, Sonnenblick LI, Gruver R, Almajano J, Bragin A, et al. (2011). Absence of CNTNAP2 leads to epilepsy, neuronal migration abnormalities, and core autism-related deficits. Cell 147, 235–246. 10.1016/j.cell.2011.08.040. [PubMed: 21962519]

Peng J, Elias JE, Thoreen CC, Licklider LJ, and Gygi SP (2003). Evaluation of multidimensional chromatography coupled with tandem mass spectrometry (LC/LC-MS/MS) for large-scale protein analysis: the yeast proteome. J Proteome Res 2, 43–50. [PubMed: 12643542]

Poliak S, Salomon D, Elhanany H, Sabanay H, Kiernan B, Pevny L, Stewart CL, Xu X, Chiu SY, Shrager P, et al. (2003). Juxtaparanodal clustering of Shaker-like K+ channels in myelinated axons depends on Caspr2 and TAG-1. J Cell Biol 162, 1149–1160. 10.1083/jcb.200305018. [PubMed: 12963709]

Poot M (2015). Connecting the CNTNAP2 Networks with Neurodevelopmental Disorders. Mol Syndromol 6, 7–22. 10.1159/000371594. [PubMed: 25852443]

Prenzel N, Zwick E, Daub H, Leserer M, Abraham R, Wallasch C, and Ullrich A (1999). EGF receptor transactivation by G-protein-coupled receptors requires metalloproteinase cleavage of proHB-EGF. Nature 402, 884–888. 10.1038/47260. [PubMed: 10622253]

Roussel C, Erneux T, Schiffmann SN, and Gall D (2006). Modulation of neuronal excitability by intracellular calcium buffering: from spiking to bursting. Cell Calcium 39, 455–466. 10.1016/j.ceca.2006.01.004. [PubMed: 16530827]

Rubio-Marrero EN, Vincelli G, Jeffries CM, Shaikh TR, Pakos IS, Ranaivoson FM, von Daake S, Demeler B, De Jaco A, Perkins G, et al. (2016). Structural Characterization of the Extracellular Domain of CASPR2 and Insights into Its Association with the Novel Ligand Contactin1. J Biol Chem 291, 5788–5802. 10.1074/jbc.M115.705681. [PubMed: 26721881]

Scott-Van Zeeland AA, Abrahams BS, Alvarez-Retuerto AI, Sonnenblick LI, Rudie JD, Ghahremani D, Mumford JA, Poldrack RA, Dapretto M, Geschwind DH, and Bookheimer SY (2010). Altered functional connectivity in frontal lobe circuits is associated with variation in the autism risk gene CNTNAP2. Sci Transl Med 2, 56ra80. 10.1126/scitranslmed.3001344.

Smith KR, Kopeikina KJ, Fawcett-Patel JM, Leaderbrand K, Gao R, Schurmann B, Myczek K, Radulovic J, Swanson GT, and Penzes P (2014). Psychiatric risk factor ANK3/ankyrin-G nanodomains regulate the structure and function of glutamatergic synapses. Neuron 84, 399–415. 10.1016/j.neuron.2014.10.010. [PubMed: 25374361]

Sonderegger P, and Matsumoto-Miyai K (2014). Activity-controlled proteolytic cleavage at the synapse. Trends Neurosci 37, 413–423. 10.1016/j.tins.2014.05.007. [PubMed: 24969462]

Srivastava DP, Woolfrey KM, and Penzes P (2011). Analysis of dendritic spine morphology in cultured CNS neurons. Journal of visualized experiments : JoVE, e2794. 10.3791/2794. [PubMed: 21775964]

Stafford N, Wilson C, Oceandy D, Neyses L, and Cartwright EJ (2017). The Plasma Membrane Calcium ATPases and Their Role as Major New Players in Human Disease. Physiol Rev 97, 1089–1125. 10.1152/physrev.00028.2016. [PubMed: 28566538]

Suzuki K, Hayashi Y, Nakahara S, Kumazaki H, Prox J, Horiuchi K, Zeng M, Tanimura S, Nishiyama Y, Osawa S, et al. (2012). Activity-dependent proteolytic cleavage of neuroligin-1. Neuron 76, 410–422. 10.1016/j.neuron.2012.10.003. [PubMed: 23083742]

Tabb DL, McDonald WH, and Yates JR 3rd (2002). DTASelect and Contrast: tools for assembling and comparing protein identifications from shotgun proteomics. J Proteome Res 1, 21–26. [PubMed: 12643522]

Takata A, Miyake N, Tsurusaki Y, Fukai R, Miyatake S, Koshimizu E, Kushima I, Okada T, Morikawa M, Uno Y, et al. (2018). Integrative Analyses of De Novo Mutations Provide Deeper Biological Insights into Autism Spectrum Disorder. Cell Rep 22, 734–747. 10.1016/j.celrep.2017.12.074. [PubMed: 29346770]

Thouvenot E, Urbach S, Vigy O, Seveno M, Galeotti N, Nguyen G, Bockaert J, and Marin P (2012). Quantitative proteomic analysis reveals protein expression changes in the murine neuronal secretome during apoptosis. J Proteomics 77, 394–405. 10.1016/j.jprot.2012.09.013. [PubMed: 23009950]

Tian L, Stefanidakis M, Ning L, Van Lint P, Nyman-Huttunen H, Libert C, Itohara S, Mishina M, Rauvala H, and Gahmberg CG (2007). Activation of NMDA receptors promotes dendritic spine development through MMP-mediated ICAM-5 cleavage. J Cell Biol 178, 687–700. 10.1083/jcb.200612097. [PubMed: 17682049]

Tien WS, Chen JH, and Wu KP (2017). SheddomeDB: the ectodomain shedding database for membrane-bound shed markers. BMC Bioinformatics 18, 42. 10.1186/s12859-017-1465-7. [PubMed: 28361715]

Tong XJ, Lopez-Soto EJ, Li L, Liu H, Nedelcu D, Lipscombe D, Hu Z, and Kaplan JM (2017). Retrograde Synaptic Inhibition Is Mediated by alpha-Neurexin Binding to the alpha2delta Subunits of N-Type Calcium Channels. Neuron 95, 326–340 e325. 10.1016/j.neuron.2017.06.018. [PubMed: 28669545]

Uhlhaas PJ, and Singer W (2006). Neural synchrony in brain disorders: relevance for cognitive dysfunctions and pathophysiology. Neuron 52, 155–168. 10.1016/j.neuron.2006.09.020. [PubMed: 17015233]

Uhlhaas PJ, and Singer W (2007). What do disturbances in neural synchrony tell us about autism? Biol Psychiatry 62, 190–191. 10.1016/j.biopsych.2007.05.023. [PubMed: 17631116]

Uhlhaas PJ, and Singer W (2010). Abnormal neural oscillations and synchrony in schizophrenia. Nat Rev Neurosci 11, 100–113. 10.1038/nrn2774. [PubMed: 20087360]

Voineagu I, Wang X, Johnston P, Lowe JK, Tian Y, Horvath S, Mill J, Cantor RM, Blencowe BJ, and Geschwind DH (2011). Transcriptomic analysis of autistic brain reveals convergent molecular pathology. Nature 474, 380. 10.1038/nature10110 https://www.nature.com/articles/nature10110#supplementary-information. [PubMed: 21614001]

Won S, Incontro S, Nicoll RA, and Roche KW (2016). PSD-95 stabilizes NMDA receptors by inducing the degradation of STEP61. Proc Natl Acad Sci U S A 113, E4736–4744. 10.1073/pnas.1609702113. [PubMed: 27457929]

Wong RK, Miles R, and Traub RD (1984). Local circuit interactions in synchronization of cortical neurones. J Exp Biol 112, 169–178. [PubMed: 6439813]

Highlights

- The neuronal sheddome is enriched in neurodevelopmental disorder risk factors
- CNTNAP2 is cleaved and its ectodomain is detectable in the cerebrospinal fluid
- Neuron activity boosts CNTNAP2 shedding and the ectodomain binds to Ca^{2+} pump PMCA2
- CNTNAP2 ectodomain enhances Ca^{2+} extrusion and reduces neuronal network synchrony

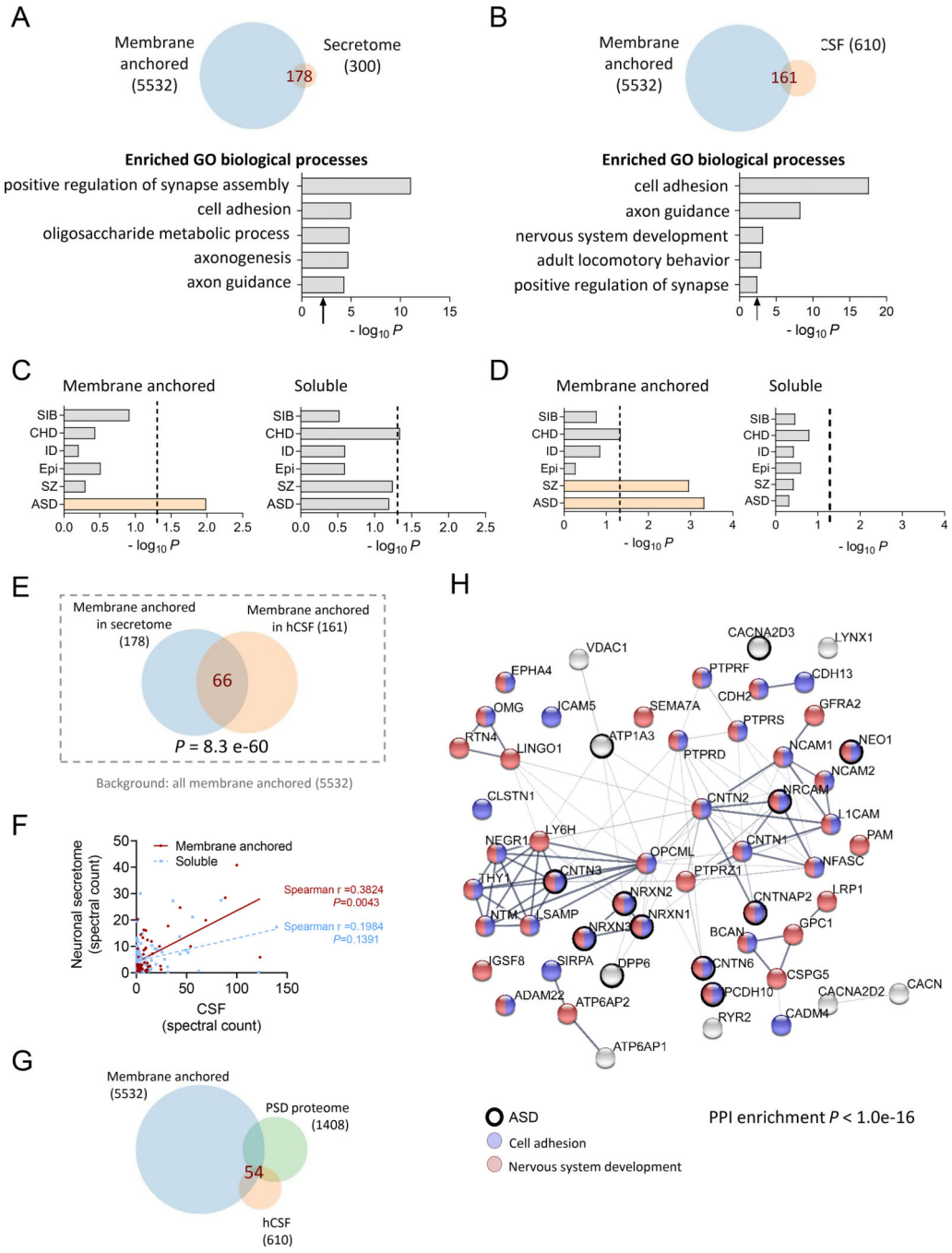

Figure 1. Computational analysis of the neuronal and hCSF sheddomes.

A. Venn diagram of proteins from *in vitro* neuronal secretome (n=300) and its membrane anchored subset (n=178) susceptible to ES. GO analysis of the neuronal sheddome. **B.** Venn diagram showing that 161 of the 610 proteins detected in hCSF could potentially undergo ES. GO analysis of membrane-anchored proteins in the hCSF. **C.** Enrichment of proteins encoded by disease-relevant genes in the membrane-anchored but not the soluble secretome fraction. **D.** Enrichment of SZ- and ASD-related genes in the membrane-anchored fraction of hCSF. **E.** Hypergeometric testing shows a highly significant overlap between

the neuronal sheddome *in vitro* and the hCSF sheddome (orange). **F.** Spectral counts of membrane-anchored proteins in the neuronal secretome are significantly correlated with the hCSF (P=0.043), while those in the soluble protein fraction are not (P=0.1391). **G.** Venn diagram defining the synaptic sheddome. **H.** PPI network of the 54 proteins in the synaptic sheddome.

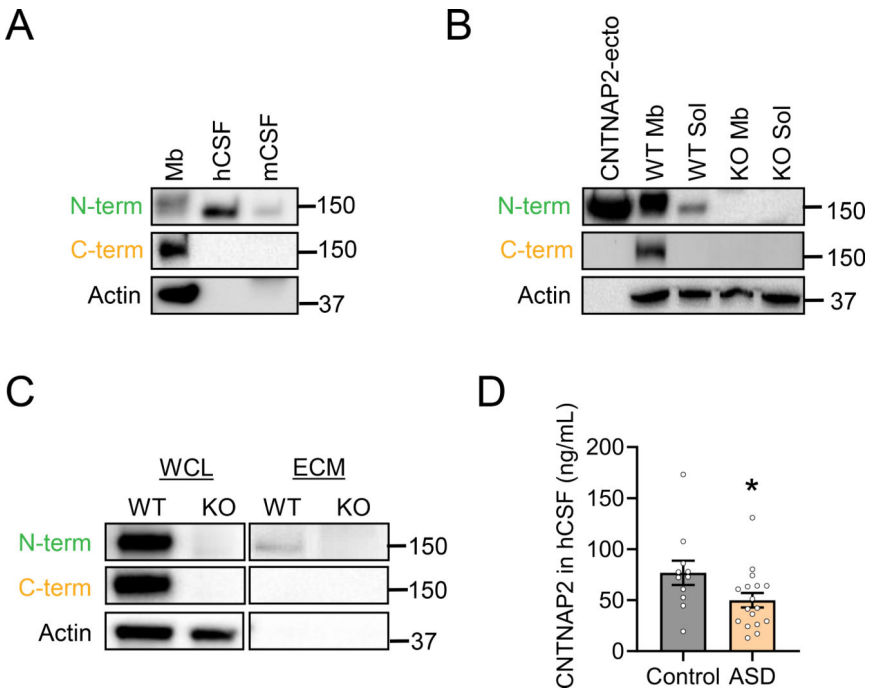

Figure 2. CNTNAP2 undergoes ectodomain shedding.

A. Western blots of mouse cortex membrane fraction (Mb), hCSF, and mCSF using N-term and C-term CNTNAP2 antibodies. **B.** Membrane and soluble fractions of *Cntnap2* WT and KO mouse cortex. Positive control is CNTNAP2-ecto produced in N2a cells. **C.** Western blots show both termini of CNTNAP2 in the whole cell lysates (WCL) from WT dissociated neurons but only N-term signal in the extracellular media (ECM); bands are absent from *Cntnap2* KO neurons. **D.** ELISA of hCSF from unaffected controls and individuals with ASD (n=11–17; control *vs.* ASD *t*-test, **P*=0.0478). Data are mean ± SEM.

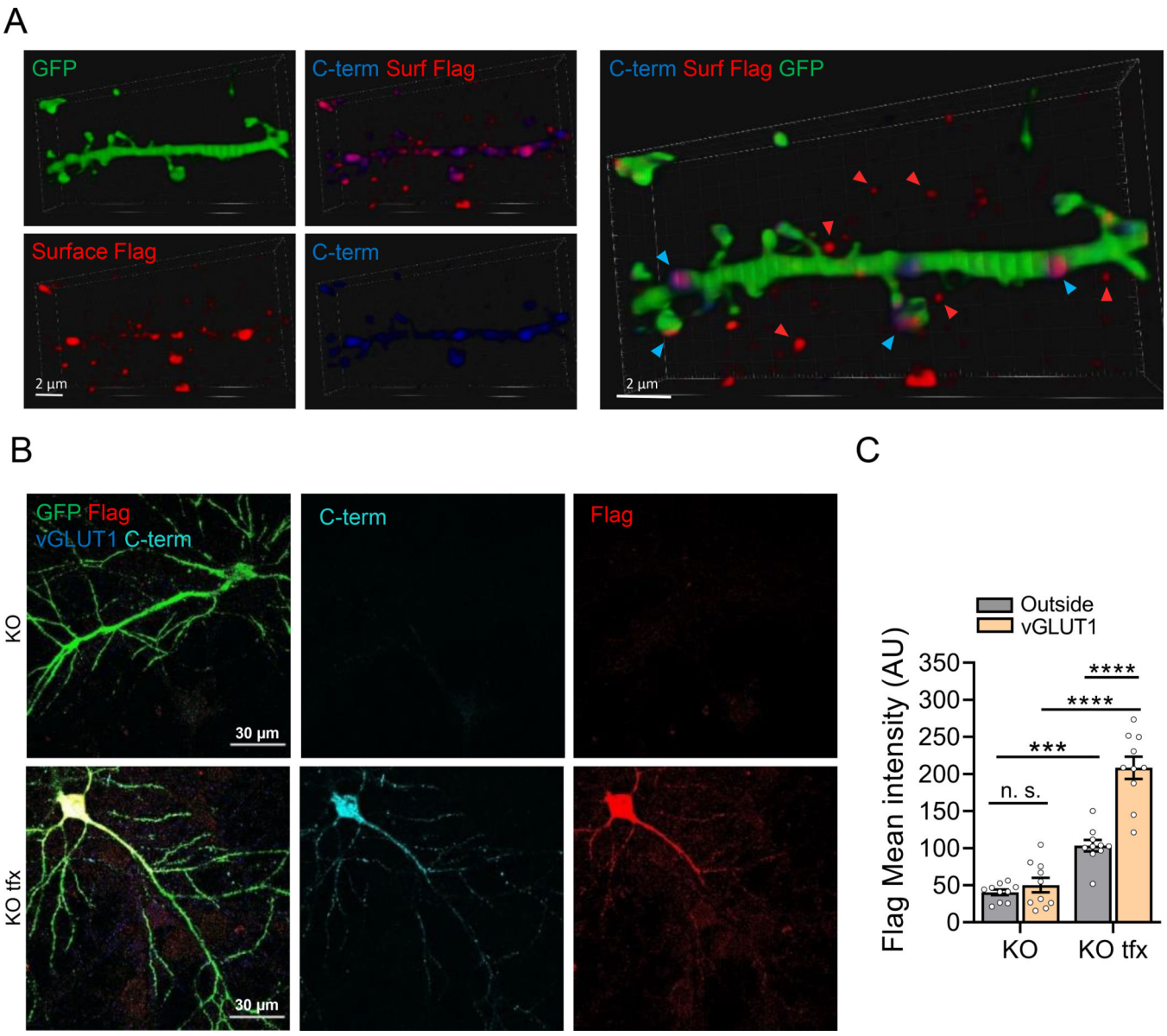

Figure 3. Spatial distribution of neuronal CNTNAP2 ectodomain shedding.

A. 3D reconstructions of confocal images of *Cntnap2* KO neurons transfected with Flag-CNTNAP2 and GFP, immunostained for Flag under non-permeabilized conditions and for GFP and C-term CNTNAP2 under permeabilized conditions. Flag and C-term colocalized on the cell surface (blue arrowheads); in the perineuronal space, only the Flag signal showed (red arrowheads). **B.** Single plane confocal imaging of *Cntnap2* KO and Flag-CNTNAP2 transfected *Cntnap2* KO neurons stained for GFP, Flag, vGLUT1, and CNTNAP2 C-term antibodies. **C.** Analysis of all Flag mean fluorescence intensity outside of transfected cells or outside but overlapping with vGLUT1. Data are mean ± SEM, (n=10; 2-way ANOVA $P<0.0001$ +Tukey *post hoc*, # $P<0.05$).

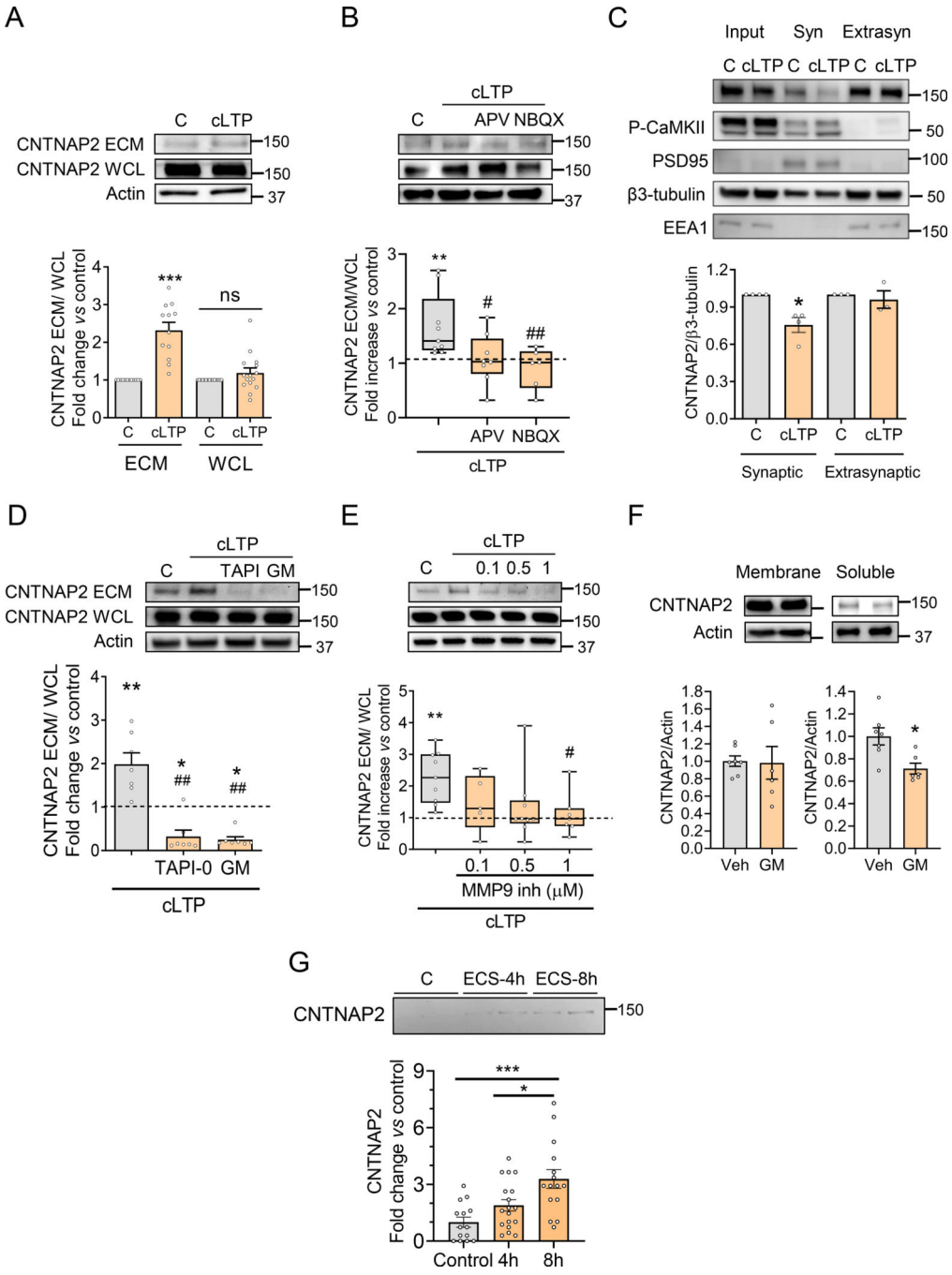

Figure 4. Activity and MMP9-dependent CNTNAP2 ectodomain shedding.

A. cLTP increases CNTNAP2-ecto levels in the ECM; no changes occur in WCL (n=12, paired *t*-test, ***P<0.0001; WCL: n=15, paired *t*-test, ^{ns}P=0.1780). **B.** APV and NBQX block cLTP-induced CNTNAP2-ecto shedding (n=6–9; control (C) *vs.* cLTP Wilcoxon test, **P=0.039; cLTP *vs.* NBQX/APV Kruskal-Wallis **P=0.0083 + Dunn's *post hoc*, $^{\#}P$=0.00387, $^{\#\#}P$=0.0089). **C.** Subcellular fractionation of rat cortical neuron cultures shows that N-term CNTNAP2 levels decrease in the synaptic fraction after cLTP (n=3–4; Synaptic C *vs.* cLTP paired *t*-test, *P=0.026; extrasynaptic C *vs.* cLTP paired *t*-test, P=0.62). **D.**

Activity-dependent CNTNAP2-ecto shedding is prevented by incubation with TAPI-0 and GM6001 (n=7; C *vs.* cLTP paired *t*-test, ***P*=0.0092; C *vs.* TAPI Wilcoxon test, **P*=0.0313, C *vs.* GM Wilcoxon test, **P*=0.015; cLTP *vs.* TAPI/GM Friedman test *P*=0.0012 + Dunn's *post hoc*, ## *P*<0.01). **E.** MMP9 inhibitor I decreases CNTNAP2-ecto shedding upon cLTP (n=5–9; C *vs.* cLTP paired *t*-test, ***P*<0.0016; cLTP *vs.* MMP9 inhibitor I Kruskal-Wallis *P*=0.022 + Dunn's *post hoc*, $^{\#}P$<0.05). **F.** Intraperitoneal administration of GM6001 (100 mg/kg) decreases CNTNAP2 levels in soluble but not in membrane fractions of mouse cortex (n=7–6, *t*-test, **P*=0.011). **G.** Western blot analysis of CNTNAP2-ecto in rat CSF collected 4 and 8h following electroconvulsive shock (ECS), as compared to non-ECS controls (n=14–18, one-way ANOVA, ****P*=0.0004 + Tukey's *post hoc* ****P*=0.0003, **P*=0.0225. Data are presented as mean ± SEM (A, C, D, F, G) or as box plots, with highest and lowest levels shown by error bars (B, E).

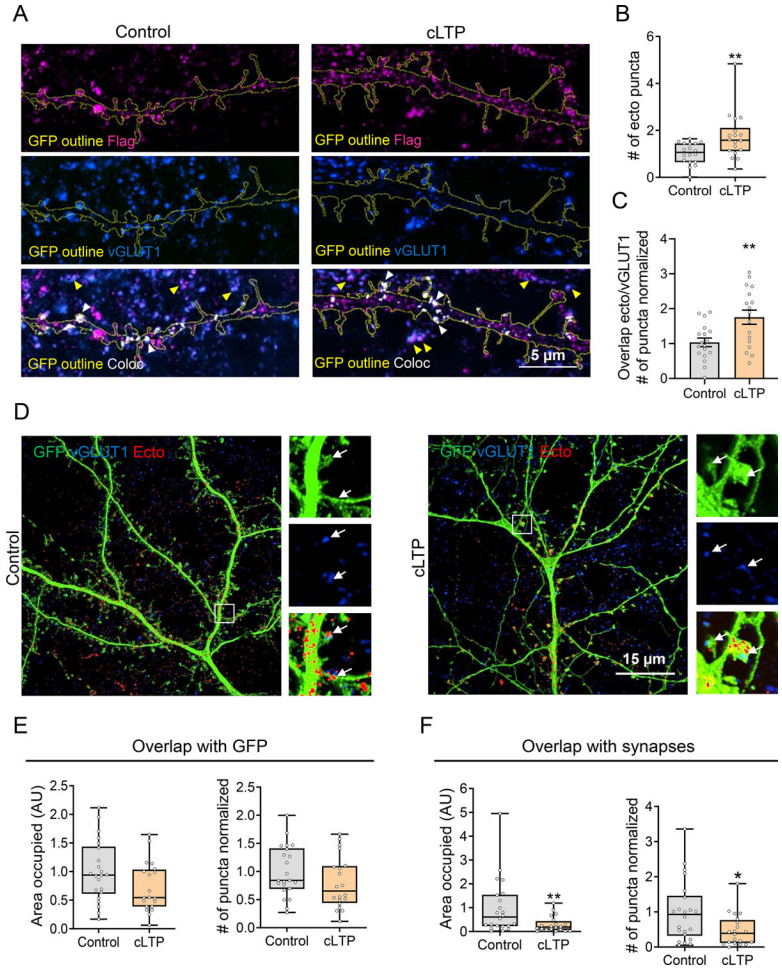

Figure 5. Activity regulates synaptic CNTNAP2-ecto shedding.

A. *Cntnap2* KO neurons transfected with GFP and Flag-CNTNAP2 were subjected to cLTP treatment, then imaged using SIM. Flag colocalized with vGLUT1 outside neurons (yellow arrowheads) and within neuronal outlines (white arrows). **B.** Number of CNTNAP2-ecto puncta in the extracellular compartment (5 um region outside GFP outline) (n=17–18 neurons, N=2 cultures, 2–3 coverslips/condition/culture. Mann-Whitney test, ***P*=0.0058). **C.** Normalized number of puncta defined by CNTNAP2-ecto and vGLUT1 overlap in the extracellular compartment (n=17–18 neurons, N=2 cultures, 2–3 coverslips/condition/culture, ***P*=0.0042). **D.** SIM image analysis without (left) or with (right) cLTP shows a decrease in CNTNAP2-ecto in synaptic regions. **E.** Area occupied by CNTNAP2-ecto in the GFP compartment (n=20–22 neurons, N=3 cultures, 2 coverslips/condition/culture, Mann-Whitney test, *P*=0.12; # of puncta in GFP, *t*-test, *P*=0.1632). **F.** Area occupied by CNTNAP2-ecto and number of puncta in the synaptic regions (Mann-Whitney test, ***P*=0.006; # of puncta in synapses, **P*=0.024). Data are presented as mean ± SEM (C) or as box plots, with highest and lowest levels shown by error bars (B, E, F).

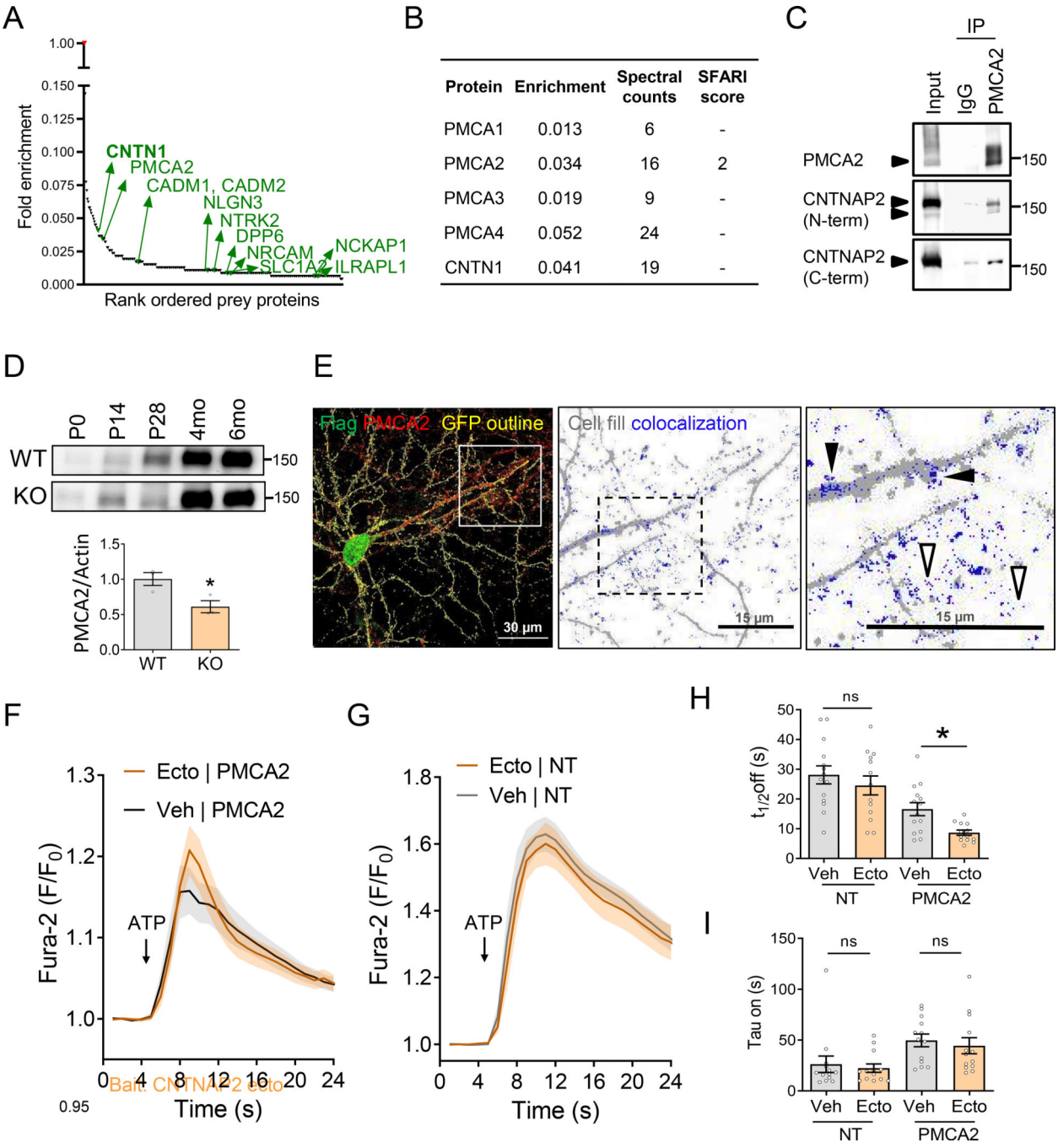

Figure 6. CNTNAP2-ecto is a binding partner and activator of PMCA2.

A. Fold enrichment of rank-ordered prey proteins detected by LC-MS/MS; ASD-related risk factors and CNTN1 are highlighted in green. **B.** Enrichment, spectral counts and SFARI score of CNTN1 and the 4 isoforms of PMCA detected by LC-MS/MS. **C.** Interaction between endogenous CNTNAP2-ecto and PMCA2 in mouse cortical membranes assessed by co-IP and western blotting. **D.** PMCA2 protein levels in *Cntnap2* WT and KO mice over time (n=3, *t*-test, **P*=0.0349). **E.** Relative distribution of Flag and endogenous PMCA2 immunofluorescence in *Cntnap2* KO neurons transfected with Flag-CNTNAP2 and

GFP. Colocalization (blue) shown relative to the cell outline. Black arrowheads indicate colocalization within dendritic regions, open arrowheads indicate colocalization outside of the neuron of origin. **F-G.** Ca^{2+} curves elicited by ATP in PMCA2-transfected or non-transfected (NT) HEK293 cells in the presence or absence of CNTNAP2-ecto. Veh, vehicle control. **H.** $t_{1/2}$ off analysis of the Ca^{2+} curve elicited by ATP in the presence or absence of CNTNAP2-ecto in PMCA2 transfected and NT HEK cells (N=6 cultures, n=13 dishes, one-way ANOVA, ***P<0.0001; Newman-Keuls *post-hoc*, *P<0.05). **I.** Comparison of tau_{on} in the ascending phase of the Ca^{2+} curve elicited by ATP (Kruskal-Wallis test, ***P=0.0004; Dunn's *post-hoc*, ^{ns}P>0.05). All data are mean±SEM.

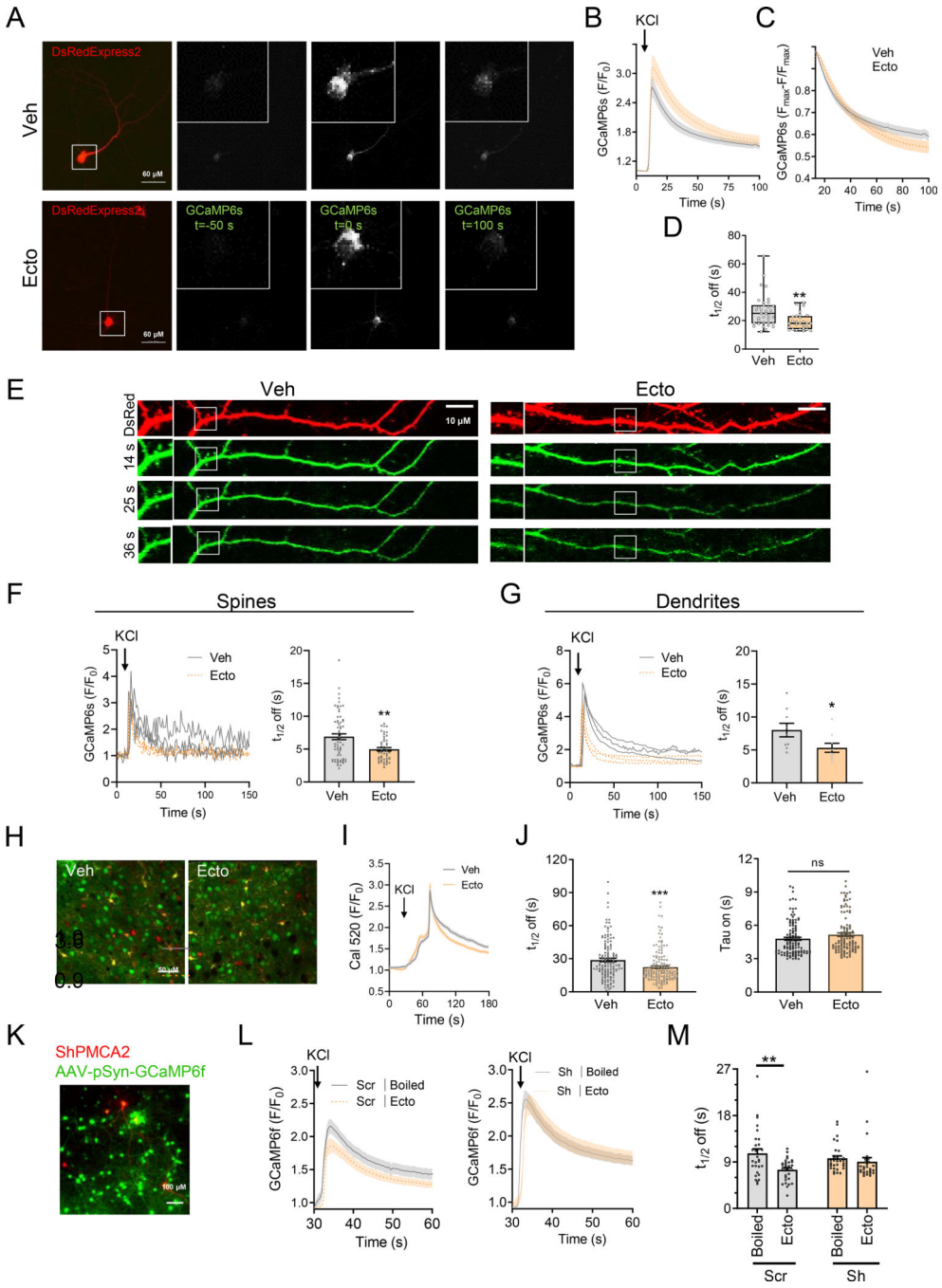

Figure 7. CNTNAP2-ecto enhances Ca^{2+} extrusion.

A. Epifluorescence images of dissociated rat neurons transfected with the Ca^{2+} indicator GCaMP6s and the cell-fill DsRedExpress2, preincubated with vehicle and CNTNAP2-ecto, imaged before and after KCl treatment. **B.** Average traces of KCl-elicited Ca^{2+} signals in somas with or without CNTNAP2-ecto incubation. **C.** Ca^{2+} decay phase normalized to maximal amplitude. **D.** $t_{1/2}$ off values of KCl-elicited Ca^{2+} peaks (N=5 cultures, n=35/28 neurons, $t_{1/2}$ off Mann-Whitney test, $^{**}P$=0.0027). **E.** Confocal images of dendrites of rat neurons transfected with GCaMP6s and DsRedExpress2, preincubated with vehicle or

CNTNAP2-ecto, imaged after KCl treatment; spines are shown in insets. **F.** Representative traces of KCl-elicited Ca^{2+} peaks in dendritic spines in CNTNAP2-ecto or vehicle-treated neurons. Bar graphs show a decrease in Ca^{2+} $t_{1/2}$ off after ecto treatment (Mann-Whitney test, N=4 cultures, n=66/49 spines and 8–9 coverslips/condition, ** P=0.077). **G.** Representative Ca^{2+} traces in dendritic shaft in CNTNAP2-ecto or vehicle-treated neurons. Bar graph shows decreased $t_{1/2}$ off in ecto-treated neurons (*t*-test, N=4 cultures, and n=9 coverslips/condition, * P=0.044). **H.** Multiphoton images showing cytosolic Ca^{2+} indicator Cal520 fluorescence in green and glial indicator SR-101 in red. **I.** KCl-elicited Ca^{2+} curves in brain slices treated with vehicle or CNTNAP2-ecto. **J.** Analysis of $t_{1/2}$ off (n=140/153 neurons, Mann-Whitney test, *** P=0.0004) and tau_{on} (n=117/116 neurons, Mann-Whitney test, ^{ns}P=0.058). **K.** Epifluorescence image of neurons infected with AAV-pSyn-GCaMP6f, transfected with mCherry PMCA2 shRNA. **L.** Average traces of KCl-elicited Ca^{2+} peaks in neurons expressing scrambled shRNA (Scr) or shPMCA2, preincubated with CNTNAP2-ecto or boiled CNTNAP2-ecto. **M.** $t_{1/2}$ off analysis (N= 1 culture, n=31 neurons, 2-way ANOVA + Tukey's *post hoc*, * P=0.034). Data are mean±SEM (F, G, K, N) or box plots, with highest and lowest levels shown by error bars (D).

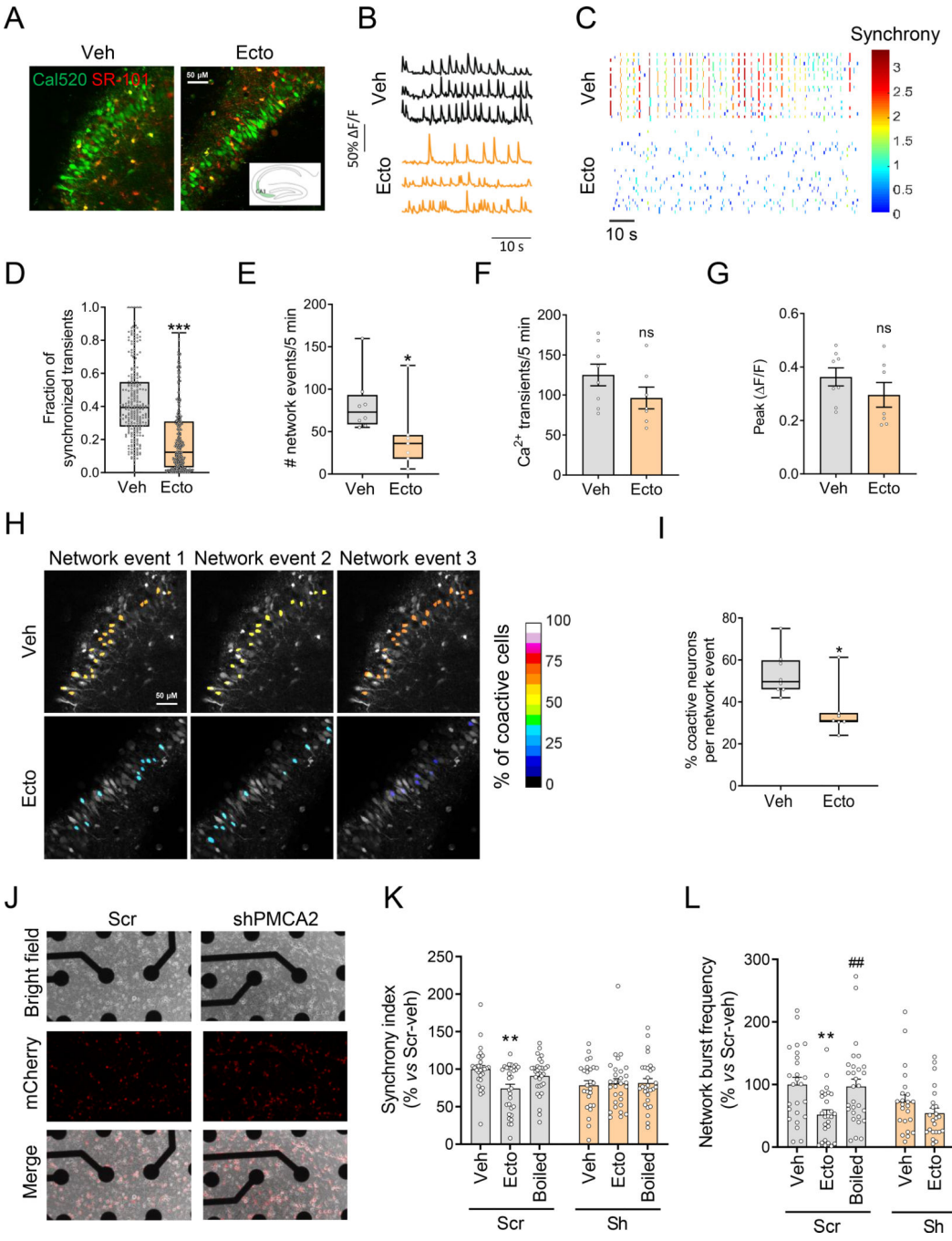

Figure 8. CNTNAP2-ecto regulates neuronal network synchrony.

A. Ca^{2+} indicator Cal520 (green) and the glial dye SR-101 (red) in the CA3 region of the hippocampus. **B.** Spontaneous Ca^{2+} signals from three neurons (from same coverslip) from vehicle-treated (black) and CNTNAP2-ecto-treated (orange) slices. **C.** Raster plot of Ca^{2+} bursts over time in the hippocampus, color coded for degree of synchrony (warmer colors correspond to increased synchrony). **D.** Fraction of synchronized transients in CNTNAP2-ecto and vehicle treated slices (n=264/328 neurons, Mann-Whitney test, $^{**}P<0.0001$). **E.** Analysis of network burst frequency (number of events/5 min) after vehicle

or ecto incubation (n=7–8 slices, N=7 mice. Mann-Whitney test, **P*=0.0140). **F.** Ca^{2+} firing frequency in vehicle and ecto treated slices (n=7/8, *t*-test, *P*=0.16). **G.** Amplitude of the Ca^{2+} peaks (n=7/8, *t*-test, *P*=0.25). **H.** Color-coded percentage of active cells in an individual Ca^{2+} burst of activity in three representative spontaneous network events occurring in the same slice in vehicle-treated or ecto-treated conditions. **I.** Percentage of coactive neurons during a Ca^{2+} burst in vehicle- or ecto-treated slices (n=810/871 neurons, Mann-Whitney test, **P*=0.014). **J.** Bright-field and mCherry immunofluorescence images of neuronal cultures on MEA plates with neurons infected with virus expressing Scr or shPMCA2. **K.** Synchrony index analysis of Scr or shPMCA2-expressing neurons cultured on MEA plates and treated with vehicle, ecto or boiled ecto (n=26–30 wells, N=6 different cultures, 2-way ANOVA *P*=0.0463, Tukey *post-hoc* test, ***P*=0.0034). **L.** Network burst frequency (n=23–29 wells, N=6 different cultures, 2-way ANOVA *P*=0.2320, Tukey *post-hoc* test, ***P*=0.0032 $^{\#\#}P$=0.0043). Data are mean±SEM (F, G, K, L) or box plots, with highest and lowest levels shown by error bars (D, E, I).

KEY RESOURCES TABLE

REAGENT or RESOURCE	SOURCE	IDENTIFIER
Antibodies		
Rabbit polyclonal anti-CNTNAP2 antibody (C-term)	Millipore	Cat# AB5886 RRID:AB_92118
Mouse monoclonal anti-CNTNAP2 antibody (N-terminal)	NeuroMab	Cat#: 75-075 RRID:AB_2245198
Mouse monoclonal anti-β-Actin antibody	Sigma-Aldrich	Cat# A2228 RRID:AB_476697
Chicken polyclonal anti-GFP antibody	Abcam	Cat# ab13970 RRID:AB_300798
Mouse monoclonal ANTI-FLAG® M2 antibody	Sigma-Aldrich	Cat# F1804 RRID:AB_262044
Guinea pig polyclonal anti-vGLUTI antibody	Synaptic System Antibodies	Cat# 135304 RRID:AB_887878
Rabbit polyclonal anti-PMCA2 ATPase antibody	Thermo Fisher Scientific	Cat# PA1-915 RRID:AB_2243199
Goat polyclonal anti-CNTNI antibody	Abcam	Cat# ab186067 RRID:AB_2747534
Rabbit monoclonal anti-β3-tubulin antibody	Cell Signaling Technology	Cat# 5568 RRID:AB_10694505
Rabbit polyclonal anti-EEA1 antibody	Cell Signaling Technology	Cat# 2411 RRID:AB_2096814
Rabbit monoclonal anti-PSD95 antibody	Cell Signaling Technology	Cat# 3450 RRID:AB_2292883
Rabbit polyclonal anti-CaMKII, phospho (Thr286) antibody	Abcam	Cat# ab32678 RRID:AB_725893
Rabbit polyclonal anti-Neuroligin 1 (extracellular) antibody	Alomone Labs	Cat# ANR-035 RRID:AB_2341006
Biological samples		
Pooled murine (CD1) CSF	Bioreclamation IVT	N/A
Remnants of human CSF	Bioreclamation IVT	Cat# HUMANCSFR-0001211
CSF controls	NIH Neurobiobank	N/A
CSF from people with ASD	NIH Neurobiobank	N/A
Chemicals, peptides, and recombinant proteins		
Lipofectamine 2000	Thermo Fisher Scientific	Cat# 11668019
Poly-D-lysine	Sigma-Aldrich	Cat# P0899
B27	Life Technologies	Cat# 17504044
DL-APV	Abcam	Cat# ab120004
cOmplete™, EDTA-free Protease inhibitor cocktail	Sigma-Aldrich	Cat# 11873580001
Phosphatase inhibitor cocktail 3	Sigma-Aldrich	Cat# P0044
Trichloroacetic acid	Sigma-Aldrich	Cat# T8657
Picrotoxin	Abcam	Cat# ab120315
Strychnine	Abcam	Cat# ab120416
Glycine	Sigma-Aldrich	Cat# 50046
NBQX	Tocris	Cat# 1044
TAPI-0	Enzo	Cat# BML-PI133-0001
GM6001	Sigma-Aldrich	Cat# 364205
MMP9 inhibitor I	Sigma-Aldrich	Cat# 444278
Anti-Flag M2 affinity gel	MilliporeSigma	Cat# A2220
Protein A/G agarose beads	Thermo Fisher	Cat# 20421

REAGENT or RESOURCE	SOURCE	IDENTIFIER
Fura-2, AM	LifeTechnologies	Cat# F1221
Adenosine 5'-triphosphate (ATP)	Sigma-Aldrich	Cat# A2383
OptiMEM	Thermo Fisher	Cat# 31985070
DMEM	Thermo Fisher	Cat# MT10013CV
CaptivA ® Protein A Affinity Resin	RepliGen	Cat# CA-PRI-0005
SR-101	Sigma-Aldrich	Cat# S7635
Cal520, AM	AAT Bioquest	Cat# 21130
Critical commercial assays		
CNTNAP2 ELISA Kit	RayBiotech	Cat# ELH-Caspr2
Deposited data		
Experimental models: Cell lines		
HEK293T	ATCC	CRL-11268 RRID:SCR_013869
Experimental models: Organisms/strains		
CD1 mice	Charles River Laboratories	Cat# CRL-22 RRID:IMSR_CRL:22
Cntnap2 KO mice	Elior Peles (Poliak et al., 2003)	N/A
Sprague Dawley male rats	Charles River Laboratories	Cat# Crl:SD RRID:RGD_737891
C57BL6J mice	Jackson Laboratories	Cat# JAX:000664 RRID:IMSR_JAX:000664
Oligonucleotides		
CNTNAP2_GT_WT_F	Peter Penzes (Gao et al., 2018)	N/A
CNTNAP2_GT_WT_R	Peter Penzes (Gao et al., 2018)	N/A
CNTNAP2_GT_Neo_R	Peter Penzes (Gao et al., 2018)	N/A
Recombinant DNA		
Flag-CNTNAP2	Peter Penzes (Gao et al., 2018)	N/A
PMCA2w/b	Gift from Emanuel Strehler	Addgene plasmid #47586 RRID:Addgene_47586
pGP-CMV-GCAMP6s	Gift from Douglas Kim	Addgene plasmid # 40753 RRID:Addgene_40753
CNTN4.2-FC-His	Gift from Woj Wojtowicz	Addgene plasmid #72068 RRID:Addgene_72068
AAV1.Syn.GCaMP6f.WPRE.SV40	Gift from Douglas Kim	Addgene plasmid #100837 RRID:Addgene_100837
pEGFP-N1	Clontech	N/A, discontinued
pDsRedExpress2-N1	Clontech	Cat# 632537
shPMCA2	VectorBuilder	VB171006-1032eez
scramble shRNA	VectorBuilder	VB171006-1034vfh
Fc-CNTNAP2$_{28\text{-}1261}$	Davide Comoletti (Rubio-Marrero et al., 2016)	N/A
Software and algorithms		
FIJI (ImageJ)	NIH	https://imagej.net/ RRID:SCR_002285
NIS-Elements	Nikon	http://www.nikon.com/products/microscope-solutions/support/index.htm RRID:SCR_014329

REAGENT or RESOURCE	SOURCE	IDENTIFIER
GraphPad Prism	GraphPad Software Inc	http://www.graphpad.com/scientific-software/prism RRID:SCR_002798
ImageLab	Bio-Rad Laboratories	https://www.bio-rad.com/en-us/product/image-lab-software RRID:SCR_014210
IMARIS viewer	Oxford instruments	https://imaris.oxinst.com/ RRID:SCR_007370
Matlab	MathWorks	https://www.mathworks.com/products/matlab.html RRID:SCR_001622
DAVID Bioinformatics Resources v6.8	Laboratory of Human Retrovirology and Immunoinformatics (LHRI)	https://david.ncifcrf.gov/ RRID:SCR_001881
STRING v10.5	STRING Consortium	https://string-db.org/ RRID:SCR_005223
Other		
Amicon Ultra 50 KDa 0.5 mL centrifugal filter devices	MilliporeSigma	Cat# UFC510096
Amicon Ultra-50 KDa 15 mL centrifugal filter devices	MilliporeSigma	Cat# UFC905024
50 kDa MWCO PES 50 mL centrifugal concentrator	Sigma Aldrich	Cat# GE28-9323-62